



Spatio-temporal heterogeneity of the wind resources over a deciduous forest in the U.S. Southeast

Matteo Puccioni¹, Sonia Wharton¹, Stephan F. J. De Wekker², Robert S. Arthur¹, Tianyi Li¹, Ye Liu³, Sha Feng³, Kyle Pressel³, Raj K. Rai³, Larry K. Berg³, and Jerome D. Fast³

Correspondence: Matteo Puccioni (puccioni2@llnl.gov) and Sonia Wharton (wharton4@llnl.gov)

Abstract. The Southeastern United States is predominantly characterized by moderately tall forests ($\approx 20 \, \text{m}$) which, by absorbing a portion of flow momentum from the Atmospheric Boundary Layer, reduce wind speeds within the rotor layer of modern wind turbines. Taller wind turbines (with hub heights greater than 100 m) are likely to experience higher wind speeds, assuming that wind resources located farther away from the ground are less affected by the forest layer. However, forest canopy drag and heterogeneity effects on wind resources at high altitude above ground have not been fully investigated in the U.S. . In this work, three sites located in a deciduous forest in the Appalachian mountains of the U.S. Southeast are investigated from September 2024 through June 2025 as part of the Lidar Experiments for Assessing Flow over Forests (LEAFF) campaign. Wind statistics are resolved both within the canopy (by a meteorological tower) and above it or in clearings (via four Doppler Lidar). A reference tall wind turbine (with a hub height of 110 m and a rotor layer spanning 45 m to 175 m) is assumed for each site to estimate the available power resource. The wind statistics considered here are the mean wind speed (U), the turbulence intensity (TI) and the cube of the mean wind speed U^3 , assumed as a proxy for the power in region II of a turbine power curve. The two dominant physical features affecting the wind, i.e. the momentum absorption at the canopy interface (quantified by the drag coefficient, C_d) and the momentum entrainment from the free atmosphere, are quantified as well based on Doppler Lidar data. The present analysis aims to: 1) quantify the monthly variability of wind resources induced by the annual cycle of leaf coverage and changes in the synoptic wind conditions; 2) quantify the correlation of canopy drag and free-atmosphere wind speed with rotor-layer wind statistics; and 3) quantify the wind resource heterogeneity between canopy and nearby forest clearing sites. The present analysis reveals that site inhomogeneities in the wind resources are still found within the bottom half of the rotor layer (i.e., up to the hub height of 110 m) of a tall wind turbine. Additionally, the examined wind resources are more correlated with the wind speed in the free atmosphere than the C_d within the rotor layer, with the only exception of the TI which shows equal correlation with these two quantities. Finally, the largest vertical extent featuring site heterogeneity is found between November and January, which corresponds to the period of minimal leaf coverage (i.e., minimum leaf area index). Overall, the present study shows that, even for tall wind turbines, the wind resources within the rotor area are affected by spatial heterogeneity in surface drag and by the seasonal transition of the canopy leaf coverage. These results have implications for the siting and operation of wind turbines in forested regions, as well as for the siting of Lidar instruments during future observational campaigns.

¹Lawrence Livermore National Laboratory, Livermore (CA), 94551, United States

²University of Virginia, Charlottesville (VA), 22904, United States

³Pacific Northwest National Laboratory, Richland (WA), 99354, United States





1 Introduction

The onshore wind energy market saw substantial growth in 2023 in the United States, with 6.5 GW of added wind capacity (Wiser et al., 2024). While there are various reasons behind this growth, the recent decrease in the cost of energy (Stehly et al., 2024), modernization of wind energy technologies (Darwish and Al-Dabbagh, 2020; Ackermann and Söder, 2000) and the increased predictive accuracy of mesoscale numerical models, such as the Weather Research and Forecasting (WRF) model (Al-Yahyai et al., 2010; Lee et al., 2019; Pryor et al., 2020), have all played a role. These advancements have helped to mitigate the risks associated with the design and installation of a new generation of wind turbines, which feature taller hub heights (103.4 m on average) and larger diameters (133.8 m on average) than previous turbine models (Wiser et al., 2024).

Despite recent growth, onshore wind energy supplied the U.S. electric energy demand by only 12% (U.S. averaged value) in 2023 (Wiser et al., 2024), with the U.S. Southeast region generating less than 1% of the wind energy supply at the state level. Low wind energy penetration in the Southeastern region is the result of several factors. First, low-wind speed synoptic conditions characterize the entire U.S. Southeast in the summer, thus limiting potential wind energy production. Second, the relatively high surface drag induced by forests tends to slow down the wind within typical turbine rotor layers (25 m to 150 m above ground). Third, the presence of the Appalachian mountains poses logistical challenges to the installation of new wind turbines. Additionally, the occurrence of hurricanes along the Southeastern shore (Konrad et al., 2013) increases the risk of wind energy investment in coastal areas.

The installation of taller turbines has the potential to overcome some of the aforementioned challenges and thus increase the viability of wind farms in the U.S. Southeast. This solution has already been successfully implemented in countries characterized by extended forest coverage, such as Germany (Blankenhorn and Resch, 2014; Bunzel et al., 2019) and Spain (López-Martínez, 2023). However, the realization of new wind energy facilities relies on the long-term, local quantification of the wind resources for potential wind farm sites, in terms of mean wind speed, wind direction and turbulence intensity (TI). This long-term quantification is still lacking in the U.S. Southeast at high-resolution (roughly 1 km or finer). In this regard, mesoscale numerical solvers, which resolve the flow over kilometer-scale grids, show limited capabilities in assessing the wind resources over forested areas due to flow complexities induced by forests and mountains (Liu et al., 2025) and uncertainties associated with the sub-grid wind farm parametrization (Fitch et al., 2012, 2013; Archer et al., 2020; Ma et al., 2022). For instance, operational weather forecasting tools generally do not have sufficient vertical resolution to resolve canopy effects or sufficient horizontal resolution to resolve forest heterogeneity or other terrain complexity. A compelling alternative would be to integrate the mesoscale model results with Large Eddy Simulation (LES) at higher resolution (Aitken et al., 2014; García-Santiago et al., 2024). However, this comes with increased computational cost and requires high-resolution in-situ observations to validate the numerical results.

From an experimental standpoint, wind resources are commonly assessed over complex terrain by relying on meteorological towers that collect single-point statistics at few heights, ranging from less than one meter above the ground up to a maximum of 100 m. Even though large networks of meteorological tower data are available in the forested U.S., such as the AmeriFlux network (Novick et al., 2018; Chu et al., 2023) and the National Ecological Observatory Network (NEON) (Metzger et al.,





2019), the heights probed by the tower sensors fall below the area swept by current and future wind turbines. One alternative is to use remote sensing Doppler Light Detection And Ranging (Lidar) to observe winds above the forest canopy. Prior studies performed by Wharton et al. (2017) and Butterworth et al. (2021) utilized nearby forest clearings to gather these observations. In the Southeast, wind Lidars have recently been used to study canopy effects on atmospheric turbulence within 300 m above a deciduous forest (Lee et al., 2025). This study showed a promising ability to quantify turbulence statistics up to the fourth order for different classes of wind speed, direction, thermal stability and cloud coverage. However, the question of site representation remains when deploying Lidar in forests. In particular, does the wind flow over a clearing represent flow over the canopy? And, moreover, which factors most influence site variability over these relatively small distances?

To address the above questions, the U.S. Department of Energy sponsored a series of field campaigns called Lidar Experiments for Assessing Flow over Forests (LEAFF), a multi-institutional research project focused on experimentally quantifying the available wind resources over two forested regions in the U.S., and providing high-fidelity observations to validate model predictions (Wharton et al., 2024). In the present study, the wind resource availability between the surface and 1 km above ground is investigated at LEAFF's U.S. Southeast location for 10 consecutive months. The data were collected at the Mountain Lake Biological Station (MLBS) in Virginia (U.S.) within a 18 m-tall deciduous forest in the Appalachian mountains.

The existing MLBS tower measurements, operated by NEON, are complemented in LEAFF through the synergistic use of in-situ and remote sensing measurements. In particular, four Doppler Lidar sensors (resolving the wind from 30 m to 1 km above the ground) were deployed at and within 2 km of the 30-m tall MLBS meteorological tower. It is noteworthy that one of the Lidar instruments was deployed on top of the NEON tower to extend the tower measurements to altitudes well above the canopy height. Although similar tower-mounted approaches have been utilized in the past (Eder et al., 2015; Mauder et al., 2021), LEAFF is, to our knowledge, the first field campaign to adopt this approach over a U.S. forested region. The instruments are deployed at three locations within and outside of the forest canopy, thereby allowing the assessment of the spatial heterogeneity of the wind resources. Additionally, the ten month long campaign (September 2024 through June 2025) allows us to connect the seasonal transition of canopy leaf coverage to the wind resource variability aloft.

With this in mind, the present analysis is aimed at three objectives. First, quantifying the monthly variability of rotor-layer wind resources induced by the annual cycle of forest senescence and month-to-month transitions of synoptic wind conditions. Second, quantifying the correlation of canopy drag and free-atmosphere wind speed with rotor-layer wind statistics. Third, investigating the presence of wind resource heterogeneity between canopy and nearby forest clearing sites and investigating the vertical extent where the inhomogeneities are present. The remainder of this work is organized as follows. In Section 2, the experimental site, the Lidar instruments and their scanning strategies are detailed. In Section 3, the methods used to quantify the wind resources are described. Finally, results are reported in Section 4 and conclusions are discussed in Section 5.

90 2 Mountain Lake Biological Station

The data presented in this Section are utilized to reconstruct the vertical profiles of three main statistics of interest for wind energy purposes, namely the mean wind speed (U), the turbulence intensity (TI) and the quantity U^3 , which is assumed to



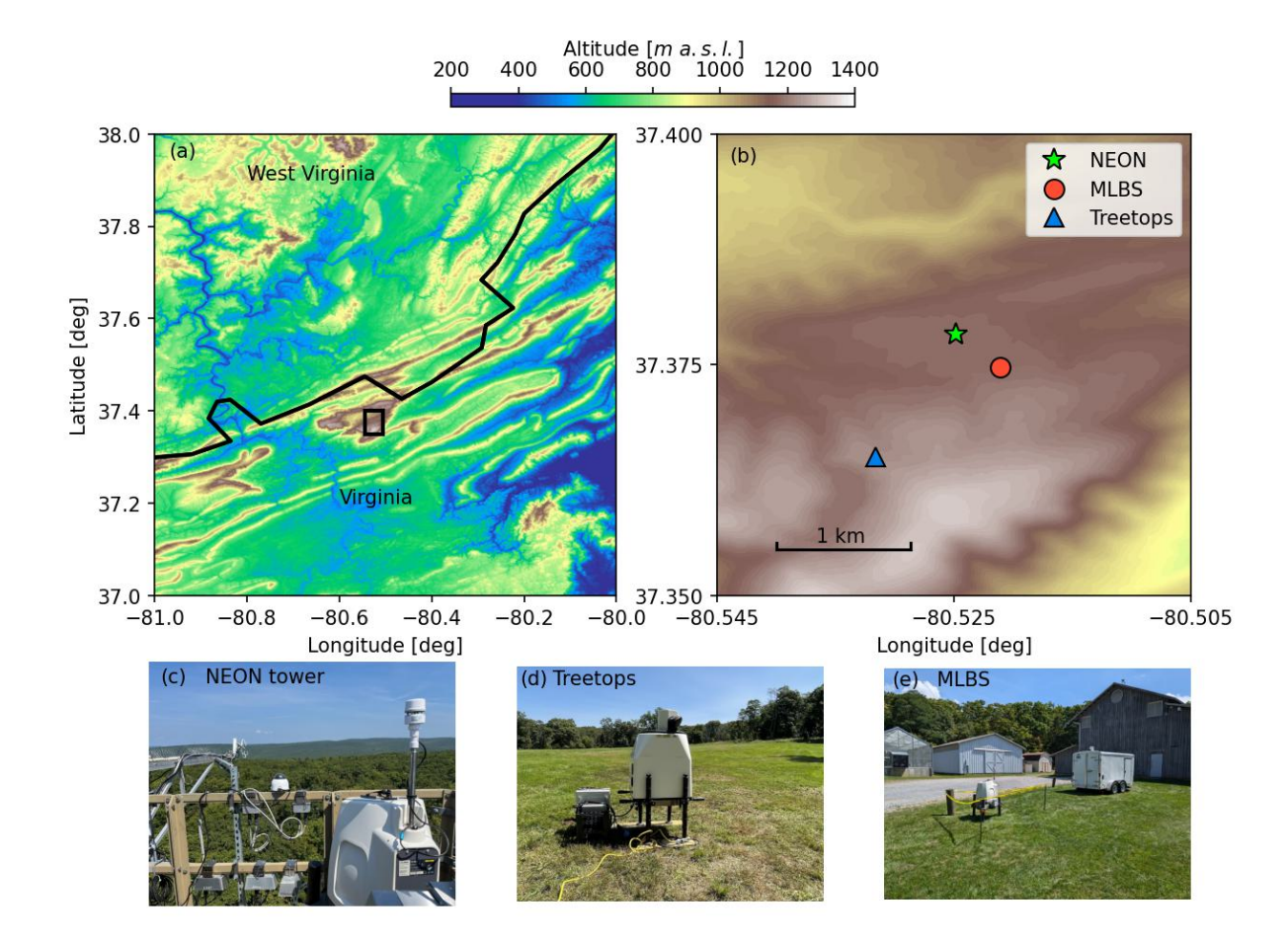


Figure 1. Overview of the experimental sites. (a) Topographic map and site location (black rectangle); the terrain elevation is provided by the U.S. Geological Survey (USGS). (b) Location of the Lidar sites; the axes limits correspond to the black rectangle in plot (a). (c) ZX-300 profiling Lidar on the 30-m tall NEON tower (measured heights, including the tower: 0.3 m to 290 m above ground). (d) Streamline XR+scanning Lidar at Treetops (measured heights: 85 m to 2 km above ground). (e) Profiling and scanning Lidars at MLBS (measured heights: 30 m to 2 km above ground).

approximate the predicted power (P) in region II of a selected wind turbine, i.e. the wind speed interval where the wind turbine is operated to maximize the power production $(P \propto U^3)$. Unless otherwise stated, the statistics are calculated over 30-minute periods simultaneously available from all the instruments.

2.1 Experimental setup

The data presented in this study have been collected during the LEAFF campaign at the Mountain Lake Biological Station (MLBS). Owned and operated by the University of Virginia (UVA), MLBS is located within a deciduous broadleaf forest with dominant species of red maple and white oak, average tree heights of h = 18 m and maximum leaf area index (LAI) of



110

115



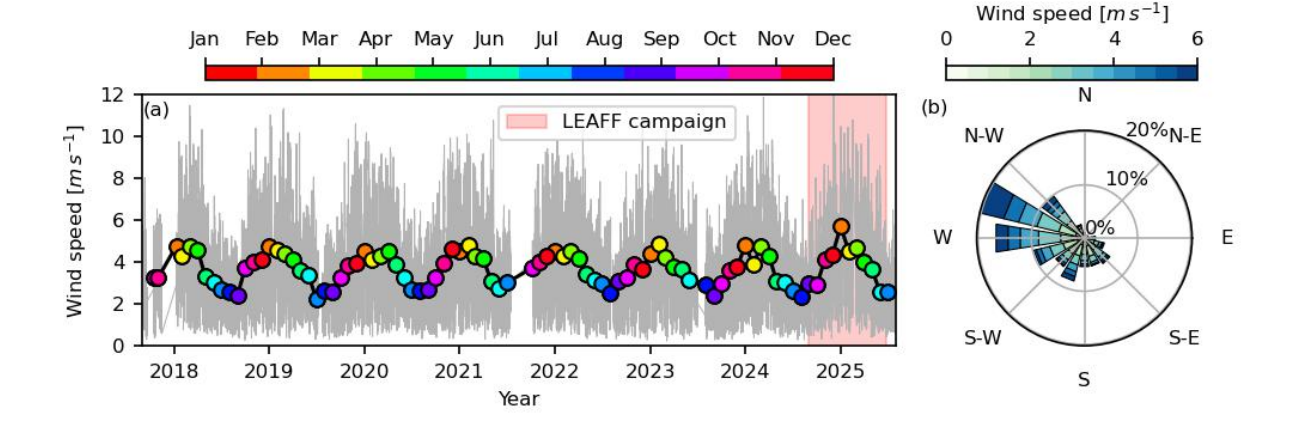


Figure 2. Multi-year wind speed at the NEON site. (a) 30-minute averaged wind speed recorded by the 3D sonic anemometer at 30 m above the ground (gray line) and monthly averaged values (circle symbols). The shaded area reports the duration of the LEAFF campaign. (b) Wind rose at NEON site based on 3D sonic anemometry.

00 LAI ≈ 2.5. Local terrain elevation varies between 900 m and 1400 m (Fig. 1b) and the site is located on a wide mountain ridge in the Appalachian mountains (Fig. 1a).

Based on site accessibility and availability of electric power, three sites in proximity of the MLBS facility are chosen for the present campaign. The first site is the 30 m-tall flux tower operated by NEON, and it is labeled as "NEON" in Fig. 1b. A 18 m-tall forest surrounds the NEON station (see Fig. 1c), thereby allowing the measurement of wind statistics developing over a large extent of forest canopy. The wind is measured by five 2D Gill ultrasonic anemometers (NEON, 2025a) used to quantify wind speed, wind direction and TI within and immediately above the canopy top (0.3 m, 4 m, 12 m, 19 m) and 24 m above ground). In addition, one CSAT-3 3D sonic anemometer is deployed at 30 m above ground (NEON, 2025b) to measure, among other variables, the mean wind speed, direction, TI, and friction velocity (u_*) at 20 Hz; here we use the 30 minute averages of these quantities. Further details about these instruments are reported in Table 1. The tower's wind profile is extended to heights well above the canopy by deploying a continuous-wave profiling Lidar (model ZX-300, manufactured by ZX Lidars) on top of the tower from August 28, 2024 to June 24, 2025 (Fig. 1c). The profiling Lidar, owned and operated by Lawrence Livermore National Laboratory (LLNL), is utilized to reconstruct wind speed, wind direction and TI by means of conical Vertical Azimuth Display (VAD) scans focused at different heights between 40 m and 290 m above the ground (cf. with Table 1), thus extending the tower data over a large range above the canopy. Details about the ZX-300 measurement technique and the uncertainties introduced in complex terrain are found in Wharton et al. (2015).

The 3D sonic anemometer data collected by the NEON tower since 2017 (NEON, 2025b) allow us to assess the presence of an average seasonal cycle in the wind speed, both within and above canopy. The seasonal cycle is reported in Fig. 2a from September 2017 to June 2025 as monthly averaged values. The maximum wind speed ($\geq 4 \,\mathrm{m\,s^{-1}}$) at 30 m occurs around February-March every year and alternates with low wind conditions ($\approx 2 \,\mathrm{m\,s^{-1}}$) during the period July-September. These







Figure 3. Leaf coverage at MLBS during 12 consecutive months captured by the phenology camera on the NEON tower. Each photo was taken around the 20th day of each month.

periods correspond with maximum (summertime) and minimum (winter and early spring) LAI across the region. The transition in LAI occurring during the LEAFF campaign is documented by the phenology camera installed on the NEON tower (Fig. 3), as part of the PhenoCam network (Richardson et al., 2018). From November through April (Fig. 3d to 3i) the forest around the NEON site is almost completely devoid of leaves, thus providing less momentum absorption from the above-canopy flow and, overall, reducing the canopy drag associated to the forest layer. In contrast, higher drag is expected from the periods





Table 1. Sites and instrumentation used during the LEAFF campaign.

Site name	GPS location	Instrument	Deployment period	Measured heights (m above ground)
NEON	N 37° 22′ 41″	profiling Lidar	Aug. 2024 - Jun. 2025	40, 50, 60, 68, 90, 110, 140, 180, 220, 260, 290
NEON		3D anemometer	Sep. 2017 - Present	30
(forest canopy)	W 80° 31′ 29″	2D anemometer	Sep. 2017 - Present	0.3, 4, 12, 19, 24
MLBS	N 37° 22′ 29″	profiling Lidar	Aug. 2024 - Mar. 2025	30, 38, 50, 60, 90, 110, 140, 180, 210, 260, 290
$(0.013\mathrm{km}^2\ \mathrm{clearing}\ \mathrm{area})$	$\mathrm{W}~80^{\circ}31^{\prime}16^{\prime\prime}$	scanning Lidar	Aug. 2024 - Present	85 to 2070 (26 m increase)
Treetops $(0.015 \mathrm{km^2} \mathrm{clearing} \mathrm{area})$	N 37° 21′ 54″ W 80° 31′ 54″	scanning Lidar	Aug. 2024 - May 2025	85 to 2070 (26 m increase)

August-October (Fig. 3a to 3c) and May-June (Fig. 3j and 3k) due to the higher foliage density present in the canopy. In 2024, 125 the day of full canopy senescence was October 31, 2024, while the leaf out was complete by May 20, 2025. From Fig. 2a and Fig. 3, the period selected for the LEAFF campaign (red shaded area in Fig. 2a) allows to resolve the entire seasonal cycle during 2024-2025, which resembles the seasonal cycle of wind speed during previous years. The wind rose, reported in Fig. 2b, reveals a prevalent West-North-West wind direction, similar to other wind farms operating along the Appalachian mountain range. The monthly-averaged distribution of wind direction (not shown here) does not feature a clear seasonal variability as 130 the wind speed does, rather it is always roughly bounded between 210° and 270° without showing any seasonal synoptic variability.

The second site chosen for the LEAFF campaign is located in a small clearing area (0.013 km²) within the MLBS facility (indicated in Fig. 1b as "MLBS" and located 500 m southeast of the NEON tower). This site is equipped with a second profiling Lidar (model ZX-300, owned by LLNL and depicted in Fig. 1e) utilized to perform conical scans in an identical manner to the ones done by the profiling Lidar atop the NEON tower. A pulsed Doppler Streamline XR+ scanning Lidar (Fig. 1e), owned by the University of Virginia (UVA) and manufactured by Lumibird, is deployed next to the profiling Lidar and utilized to further extend the probed wind speed throughout the entire Atmospheric Boundary Layer (ABL) by means of 30 minutes-long 6-points Vertical Azimuth Display (VAD) repeated every hour (cf. with Table 1).

The last site chosen for the LEAFF campaign (1.6 km southwest of the NEON tower) is a clearing area with similar extension 140 as MLBS (0.015 km²) named Treetops. This site is equipped with a second Streamline XR+ scanning Lidar (owned by LLNL and depicted in Fig. 1d) utilized to perform 6-points VAD scans as the UVA scanning Lidar at MLBS. The two scans are set to start at the beginning of each hour and last for 30 minutes. This is achieved by using the "daily scan schedule" option available in the Streamline XR+ software, thereby providing synchronized wind statistics at the two sites. For both scanning Lidars, the remaining 30 minutes are utilized to perform vertically staring scans, whose results are out of the scope of the present study. 145



155

160

165



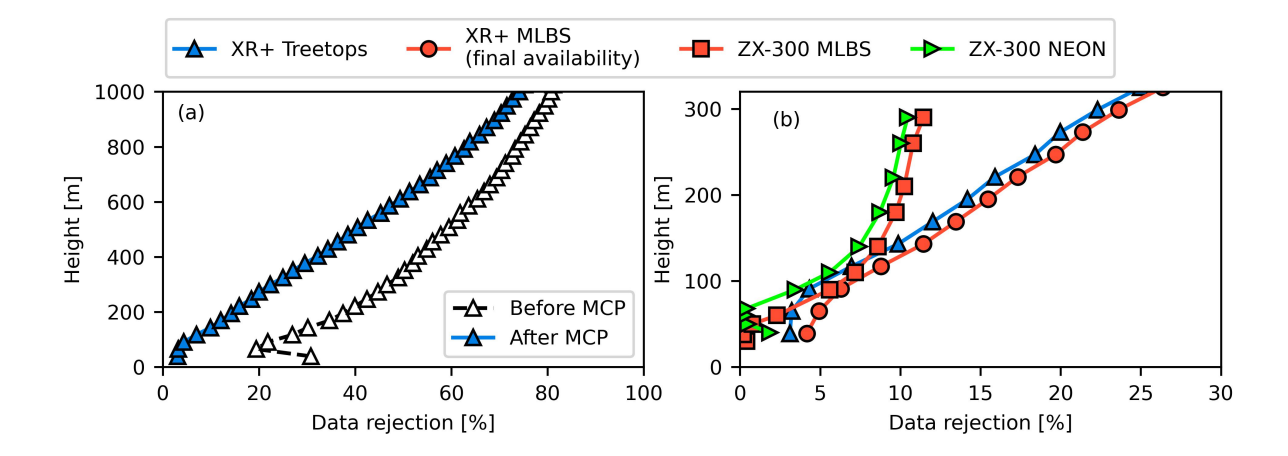


Figure 4. Percentage of data rejection at each scanned height before synchronization. (a) Data availability before and after applying the MCP algorithm to the Treetops scanning Lidar data. (b) Scanning and profiling Lidar data availability.

2.2 Quality control of the Lidar data

Focusing on the profiling Lidar data first, this instrument collects time records of horizontal and vertical wind speed and wind direction sampled every 16 s to complete a full conical scan. The velocity records are considered only for the first 30 minutes within each hour simultaneous to the scanning Lidars VAD scan. For each 30 -minute subset, instantaneous wind speed samples outside of the interval $[0, 30] \text{ m s}^{-1}$ are considered non-physical values and are removed from further analysis. The mean horizontal and vertical velocity, mean wind direction and TI are then evaluated based on the algorithm described in Section 3.1.

For scanning Lidar data, instantaneous radial wind data characterized by signal-to-noise ratio (SNR) outside of [-18, 10] dB are flagged as incorrect reads and removed. It is noteworthy that the high threshold limit (10 dB) automatically excludes the data collected within clouds since they are typically associated with higher SNR. Subsequently, for each day and month, the radial wind data from each beam are clustered by hour and the algorithm of Foken et al. (2004) is implemented to remove spikes from the data. Specifically, given a generic timeseries x(t), this algorithm flags all the instantaneous samples outside of the interval: $X \pm a \overline{x'x'}^{0.5}$, where X is the time average of x(t) and $\overline{x'x'}^{0.5}$ is the standard deviation. The constant a is chosen here as 2.5, which is lower than the value prescribed by Foken et al. (2004) (a = 3.5), thereby leading to a more restrictive data selection process. The instantaneous zonal, meridional and vertical velocity components are then calculated from the quality-controlled radial wind speed values following the algorithm described in Section 3.1.

The percentage of data rejection due to the quality control is reported in Fig. 4 within the height interval of interest. It is noticed that the XR+ Lidar located at Treetops exhibits significantly higher rejection percentage (20% to 80%) than the other instruments (<1% to 30%). This is due to several power outages occurring at the Treetops site, including a longer delay in the power recovery here than at the other two sites after Hurricane Helene in September 2024. To bring the data availability





Table 2. Scan parameters provided to perform the 6-point VAD scan by the scanning Lidars.

	LLNL	UVA	
Azimuth (θ) [$^{\circ}$]	[0, 72, 144, 218, 290, 360]		
Elevation (ϕ) [$^{\circ}$]	[60, 60, 60, 60, 60, 90]		
Gate length [m]	30	30	
Duration of VAD scan	$28^{\prime}25^{\prime\prime}$	$26^{\prime}33^{\prime\prime}$	

at the same level as the other instruments, a Measure Correlate Predict (MCP) algorithm is implemented assuming the XR+Lidar at MLBS as reference and the Treetops Lidar as target. The chosen MCP algorithm is the variance ratio method detailed in Rogers et al. (2005), which has been proven able to correctly retrieve onshore wind resources at a target site based on those available at a reference site within several hundreds of kilometers. Further details about this method are reported in Appendix B. After applying this algorithm, the data availability at Treetops is significantly increased (Fig. 4a) and brought at the same level of the remaining instruments, i.e. above 70% for the height interval of interest.

Finally, a further down-selection is made to consider only time periods when statistics are available from all the instruments for all the probed heights below 600 m above the ground. Although this step increases the statistical uncertainty, it is necessary to keep consistency between the statistical quantities retrieved at different sites. The final percentage of data rejection is reported in Fig. 4b with orange circle symbols.

3 Methods

175

3.1 Retrieval of the wind speed components from VAD scans

The radial wind data collected by the scanning Lidars (after the quality control detailed in Section 2.2) are utilized to reconstruct the time records of the three-component velocity vector at each scanned height via 6-point VAD scans, whose details are reported in Table 2. Assuming spatial homogeneity within the scanning cone, the instantaneous radial wind speed (v_r) recorded by the i-th beam (i = 1, ..., 6) at a vertical distance z is related to the three-component velocity vector by:

$$v_{r,i}(z,t) = u_{WE}(z,t)\sin\theta_i\cos\phi_i + v_{SN}(z,t)\cos\theta_i\cos\phi_i + w(z,t)\sin\phi_i, \tag{1}$$

where $u_{\rm WE}, v_{\rm SN}, w$ are the zonal, meridional and vertical velocity components, respectively, and ϕ, θ are the elevation angle (measured from the horizontal) and the azimuth angle (measured from true North), respectively. Equation (1) can be recast in vector form as:

$$\begin{pmatrix} v_{r,1} \\ \vdots \\ v_{r,6} \end{pmatrix} = \underbrace{\begin{bmatrix} \sin \theta_1 \cos \phi_1 & \cos \theta_1 \cos \phi_1 & \sin \phi_1 \\ \vdots & \vdots & \vdots \\ \sin \theta_6 \cos \phi_6 & \cos \theta_6 \cos \phi_6 & \sin \phi_6 \end{bmatrix}}_{\mathbf{k}} \begin{pmatrix} u_{\mathrm{WE}} \\ v_{\mathrm{SN}} \\ w \end{pmatrix} \rightarrow \mathbf{v}_r(z,t) = A\mathbf{u}(z,t), \tag{2}$$



190

215



where A is a 6×3 matrix whose values are determined by the azimuth and elevation angles, $\mathbf{v}_r = (v_{r,1}, ..., v_{r,6})$ and $\mathbf{u} = (u_{\text{WE}}, v_{\text{SN}}, w)$. The system (2) features six equations (one for each Lidar beam) and three unknowns (i.e. the velocity components), and it is resolved via least-squares minimization (following the algorithm of Päschke et al., 2015) to obtain the following expression of the instantaneous velocity components (Letizia et al., 2024):

$$\mathbf{u}(z,t) = (A^T A)^{-1} A^T \mathbf{v}_r(z,t). \tag{3}$$

The mean velocity, calculated for each 30-minute period, is quantified as:

$$U(z) = \sqrt{\overline{u_{\text{WE}}(z,t)}^2 + \overline{v_{\text{SN}}(z,t)}^2},$$
(4)

where the overbar indicates the time average (see, e.g., Mahrt et al., 2001). The mean wind direction from North (Θ) is then evaluated based on $\overline{u_{\rm WE}(z,t)}$ and $\overline{v_{\rm SN}(z,t)}$, and used to rotate the instantaneous velocity components $(u_{\rm WE}(z,t)$ and $v_{\rm SN}(z,t)$) into the streamwise and spanwise velocity components (u and v), the latter oriented in order to have: $\overline{u(z,t)} = U(z)$ and $\overline{v(z,t)} = 0$. This reference frame is then tilted along the spanwise direction to have zero-averaged vertical velocity component, w. The turbulence intensity is calculated based on the streamwise velocity variance $(\overline{u'u'}(z))$ as:

$$TI(z) = \sqrt{\frac{\overline{u'u'(z)}}{U^2(z)}}.$$
(5)

The profiling Lidars return the instantaneous wind direction, horizontal and vertical wind speed as a result of an internal retrieval algorithm based on 50 azimuth angles scanned at a sampling time of ≈ 16 s. The mean velocity is calculated at each height as the time average of the instantaneous values, as well as the mean wind direction. The latter is then utilized to calculate the streamwise and spanwise velocity components and, finally, the profiling Lidar's TI is calculated following Eqs. (4) and (5).

3.2 Reference wind turbine and reference wind speed

The reference turbine chosen to predict the available power is the International Energy Agency (IEA) 3.4 MW wind turbine (Bortolotti et al., 2019), whose main parameters are reported in Table 3 and whose power curve is reported in Fig. 5. The IEA 3.4 MW wind turbine features hub height and diameter comparable to those previously chosen for the operating wind farms closest to MLBS, i.e. Beech Ridge ($D = 77 \, \text{m}$, $H = 80 \, \text{m}$), Beech Ridge II ($D = 127 \, \text{m}$, $H = 89 \, \text{m}$) and Laurel Mountain ($D = 91 \, \text{m}$, $H = 80 \, \text{m}$) in West Virginia, U.S. (Hoen et al., 2018). Furthermore, the IEA 3.4 MW turbine diameter and hub height assume similar values as those chosen for the forthcoming Rocky Forge wind farm project ($D = 140 \, \text{m}$, $H = 137 \, \text{m}$) which is planned to start in 2026.

To assess the validity of the present choice of wind turbine model, the normalized probability density function (PDF) of hub-height wind speed ($U_{\rm hub}$) is calculated based on 10-minute average Lidar data at z=110 and reported in Fig. 5 for all the tested sites. The percentage of data within each operating region is also reported in Table 4. The latter, together with Fig. 5, indicates that the IEA $3.4\,\mathrm{MW}$ turbine would operate in region II for the majority of the time, thereby corroborating the present choice of reference wind turbine model.





Table 3. Main parameters of IEA 3.4 MW reference wind turbine. SL and PL stand for scanning Lidar and profiling Lidar, respectively. The diameter and hub height normalized by the canopy height (h = 18 m) are reported in parenthesis.

Name	Value		
Diameter (D) [m]	130 (7.2h)		
Hub height (H) [m]	110(6.1h)		
Rated power [kW]	3370		
Cut-in wind speed [m/s]	3		
Rated wind speed [m/s]	9.8		
Cut-out wind speed[m/s]	25		
Lidar points within rotor (N_h)	5 (Treetops), 5 (MLBS-SL) 5 (MLBS-PL), 6 (NEON)		

Table 4. Percentage of 10-minute averaged hub-height wind speed occurrences within each operative region of the IEA 3.4 MW wind turbine.

Region I (%)	Region II (%)	Region III (%)
11.7	60.6	27.7
14.9	58.5	26.6
15.4	61.7	22.9
	11.7 14.9	11.7 60.6 14.9 58.5

To quantify the power captured within the rotor area, the International Electrotechnical Commission (IEC) standard prescribes to utilize $U_{\rm hub}$ as input to the power curve (IEC, 2019), assuming $U_{\rm hub}$ as constant throughout the rotor area. However, as it will be detailed in Section 4, the mean wind profiles at the selected sites exhibit high shear which invalidates the hypothesis of constant velocity within the rotor area and, thus, may lead to incorrect estimates of the wind resources (Van Sark et al., 2019). Thus, in addition to $U_{\rm hub}$, the rotor equivalent velocity ($U_{\rm eq}$) is adopted as well:

$$U_{\text{eq}} = \left[\frac{4}{\pi^2 D} \int_{r=0}^{D/2} \int_{\varphi=0}^{2\pi} U^3(r,\varphi) r dr d\varphi \right]^{1/3}, \tag{6}$$

where D is the turbine diameter, r is the radial distance along the blade and φ is the angular position. Due to the discrete spacing of the Lidar heights within the rotor, Equation (6) is approximated through a rectangular discretization:

225
$$U_{\text{eq}} \approx \left[\frac{4}{\pi D^2} \sum_{i=1}^{N_h} U^3(z_i) A_i \right]^{1/3}$$
 (7)

where N_h is the number of scanned heights within the rotor (cf. with Table 3) and A_i is the portion of the rotor area centered around each height, z_i (Scheurich et al., 2016).



235

245

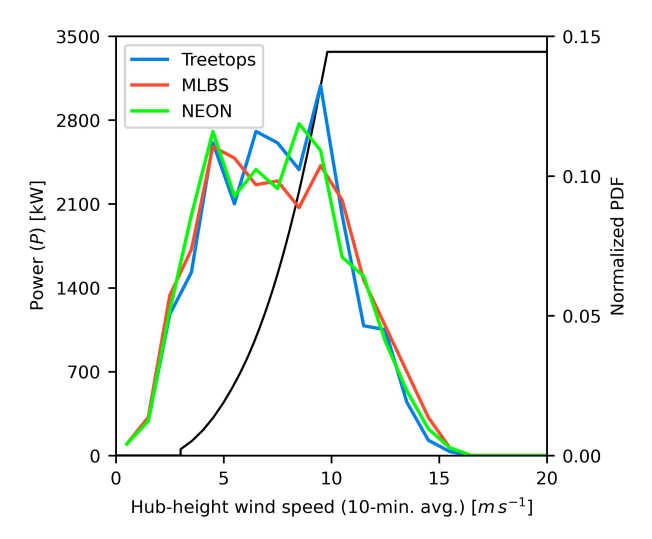


Figure 5. IEA 3.4 MW power curve (left axis) overlapped with the normalized probability density function of hub-height wind speed at the tested sites (right axis).

3.3 Mean wind speed model for canopy flows

In Section 4.3 each site will be characterized in terms of the local canopy roughness and its subsequent effect on the mean velocity profile. The canopy roughness is introduced in the analysis by selecting a mean velocity model involving a roughness parameter that must be calibrated on the experimental data. In this scenario, several models are available in literature to predict the mean wind speed above the roughness layer, namely the logarithmic law (e.g., Monin and Obukhov, 1954; Van Wijk et al., 1990; Arnqvist et al., 2015; Segalini et al., 2013), the power law (e.g., Peterson and Hennessey Jr, 1978; Gualtieri and Secci, 2012; Ryu et al., 2025), as well as empirical (Macdonald, 2000; Lalic et al., 2003) and machine learning models (Optis et al., 2021). Among them, the power law has been proven to be a reliable model applicable over hundreds of meters above the ground (Mohandes and Rehman, 2018). In this work, the power law model is adopted to estimate the mean velocity (*U*) as:

$$\frac{U(z)}{U_1} = \left(\frac{z-d}{z_1-d}\right)^{\alpha},\tag{8}$$

where U_1 is the mean wind speed at a reference height, assumed here as the lowest height above the forest canopy, α is the shear exponent and d is the displacement height. The parameters α and d are calibrated at each site for each 30-minute dataset over heights below the rotor top tip (175 m) via least-squares fitting.

With respect to the classic power law formulation (which does not account for the displacement height), introducing d in Eq. (8) is necessary to account for the vertical shift induced by the tall canopy layer. A similar approach is found for the logarithmic law of mean velocity for above-canopy flows (see, e.g., Segalini et al., 2013). The logarithmic law constitutes a more physically robust choice to model the profile of mean velocity above the canopy. However, the best-fit of the logarithmic law's parameters (friction velocity, displacement height and aerodynamic roughness) strongly depends on the vertical interval



250

255

260

265



of validity of the logarithmic law, which are typically assumed between z=h to $z\approx 5h-6h$ (i.e. $90\,\mathrm{m}$ to $108\,\mathrm{m}$) (Finnigan et al., 2009; Arnqvist et al., 2015). For the present study, the most rigorous way to assess these vertical limits would be to quantify the profiles of turbulent shear stress $(\overline{u'w'})$ and quantify the vertical interval where these profiles are constant. Since we lack the necessary 3D sonic anemometer observations to calculate this, the only measurements available to calculate $\overline{u'w'}$ are based on the Lidar. The Lidar's VAD scan technique, however, heavily underestimates $\overline{u'w'}$ due to the cross-contamination of the velocity components for different line-of-sight, and due to the averaging within the probe volume (Letizia et al., 2024). Thus, we expect the quantification of d via logarithmic law to be be less accurate than using the power law expressed by Eq. (8). In addition, the accuracy of the power law has been proven to extend over $z>100\,\mathrm{m}$ above the ground (i.e. above 5.6h), and to be superior to the logarithmic law's accuracy for thermally neutral conditions (Newman and Klein, 2014). Finally, the logarithmic law requires streamwise homogeneity to be applied (Monin and Obukhov, 1954), an assumption that may not be verified for flows over complex terrains. Thus, for the present study the power law is thought to be more feasible to model the mean wind profile above the canopy.

3.4 Quantification of the canopy drag coefficient and wind speed in the free atmosphere

The availability of quality-controlled wind statistics allows quantifying how the wind resources are affected by the two main physical mechanisms driving the flow, i.e. the momentum entrainment from the upper ABL and the momentum loss at the canopy interface. The latter is quantified by the drag coefficient (C_d) calibrated over each 30-minute period while, on the other hand, the entrainment of momentum from the free atmosphere is approximated by the wind speed probed by the scanning Lidars at 1 km above the ground (\tilde{U}), i.e. sufficiently far from the canopy to assume no correlation with the drag generated at the canopy top. The effect of canopy drag and momentum entrainment on the wind resources is quantified by calculating the correlation coefficient (ρ) of U, TI and U^3 (in region II) with either C_d or \tilde{U} . The correlation coefficient is defined as:

$$\rho(x,y) = \frac{\overline{(x-\overline{x})(y-\overline{y})}}{\overline{x'x'}^{0.5}},$$
(9)

where x and y are two generic random processes simultaneously sampled.

For each 30-minute dataset, the drag coefficient is calculated as (Yi, 2008):

$$C_d = 2\frac{|\overline{u'w'}|_h}{U_h^2},\tag{10}$$

where the subscript "h" indicates that both the turbulent stress $(\overline{u'w'})$ and the mean wind speed are evaluated at the canopy height. For the NEON site, U_h is approximated by the values measured at $z=19\,\mathrm{m}$ by the 2D sonic anemometer. For each 30-minute dataset recorded at NEON, the shear stress at the canopy top is linearly extrapolated from the $\overline{u'w'}$ profiles probed by the profiling Lidar within the interval $40\text{-}140\,\mathrm{m}$, corresponding to the lowest 7 measured heights. Due to the predicted under estimation done by the Lidar on the shear stress, the $\overline{u'w'}$ values obtained through this procedure are first extrapolated at the height probed by the 3D sonic anemometer height (30 m) and assessed against the friction velocity ($u_* = |\overline{u'w'}|^{0.5}$). The result, visualized in Fig. 6 as linear regression analysis for each month of data, indicates a strong correlation between $\overline{u'w'}$ estimated



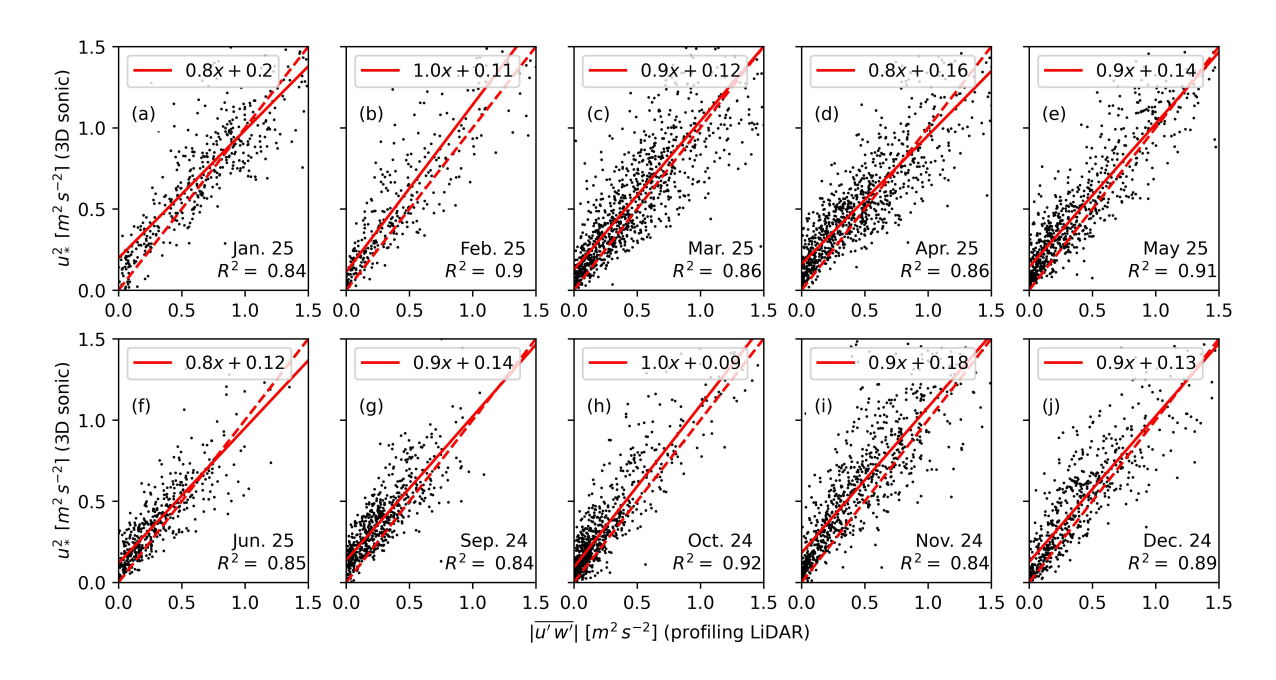


Figure 6. Monthly linear regression between turbulent shear stress at z = 30 m extrapolated from profiling Lidar (abscissa axes) and measured by the 3D sonic anemometer (ordinate axes). The 1:1 line is added for reference (red dashed line).

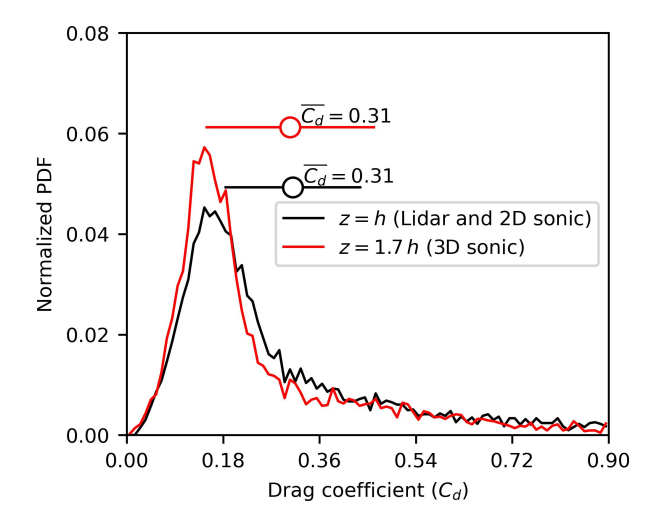


Figure 7. Histogram of drag coefficient values evaluated either based on 3D sonic anemometry (red line) or Lidar data (black line) at the NEON site. For each distribution, the symbol and uncertainty intervals report the mean and standard deviation, respectively.

from the Lidar and 3D sonic u_*^2 (R-square: 0.84 to 0.92), yet an intercept is present due to the limited spatial resolution of the Lidar. Thus, for each month of data, the turbulent shear stress values initially extrapolated from the Lidar ($\overline{u'w'}_{Lidar}$) at 30 m





Table 5. Mean wind speed, capacity factor (CF) and power law parameters at the tested sites. The reported values are based on 10-minute averaged velocity.

Site	Displace	ment height (d) [m]	Shear exponent (α)		Reference velocity [m s ⁻¹]		Capacity factor [%]	
	Mean	St. dev.	Mean	St. dev.	Mean	St. dev.	Mean	St. dev.
T	0.7	F 0	0.07	0.27 0.16	$U_{\mathrm{hub}} = 7.76$	3.04	53.9	38.0
Treetops	9.7	5.6	0.27		$U_{\rm eq} = 7.79$	3.05	54.1	38.1
MLBS	10.0	5.2	0.26	.26 0.14	$U_{\mathrm{hub}} = 8.13$	3.38	57.0	39.2
MLBS	10.0	5.2	0.20		$U_{\rm eq} = 8.13$	3.37	57.0	39.1
NEON	12.3	5.2	0.21	0.31 0.15	$U_{ m hub} = 7.75$	3.11	52.9	38.1
NEON	12.3	∂. 2	0.31		$U_{\rm eq} = 7.63$	3.05	51.7	37.9

height are corrected to obtain a closer estimate of the true turbulent stress at the canopy height $(\overline{u'w'}_h)$:

$$280 \quad |\overline{u'w'}|_h = m|\overline{u'w'}|_{\text{Lidar}} + q. \tag{11}$$

Although the slope (m) and intercept (q) are evaluated at 30 m height (i.e. 1.7 times the canopy height), wind tunnel tests previously indicated that the shear stress between h and 2h (i.e. within $z=18\,\mathrm{m}$ and $36\,\mathrm{m}$) can be assumed as constant (Segalini et al., 2013). Thus, we feel confident that Equation (11) can be used to extrapolate the shear stress at the canopy top. After evaluating C_d for all the 30-minute datasets throughout the LEAFF campaign, the normalized PDF of drag coefficient is reported in Fig. 7, either based on Lidar or 3D sonic measurements. The mean C_d value (0.32) is in agreement with previous studies which quantified directly the drag coefficient over forests (Mahrt et al., 2001; Cescatti and Marcolla, 2004; Kane and Smiley, 2006). The observed variability of the C_d (ranging from < 0.1 to 0.9) will be motivated in Section 4.1 by the monthly

4 Results

285

290

4.1 Overview of the wind resources

variations in the leaf area coverage.

4.1.1 Mean wind speed parameters and predicted power

The wind statistics at the tested sites are quantified by the profiles of mean wind speed and TI averaged across the entire duration of the LEAFF campaign (Fig. 8). The uncertainty intervals reported in Fig. 8 are calculated as: σ/\sqrt{N} , where σ is the standard deviation of the considered quantity and N is the number of samples used to obtain the statistic. From Fig. 8a, differences in the above-canopy velocity profiles are observed among the three sites up to $z \approx 100\,\mathrm{m}$ (corresponding to 5.6h), thus within the rotor area of the modeled wind turbine (45 m to 175 m). Below $100\,\mathrm{m}$ (Fig. 8c) the NEON site is characterized by lower wind speed than the other sites. The NEON site is also characterized by larger TI than the MLBS and Treetops sites





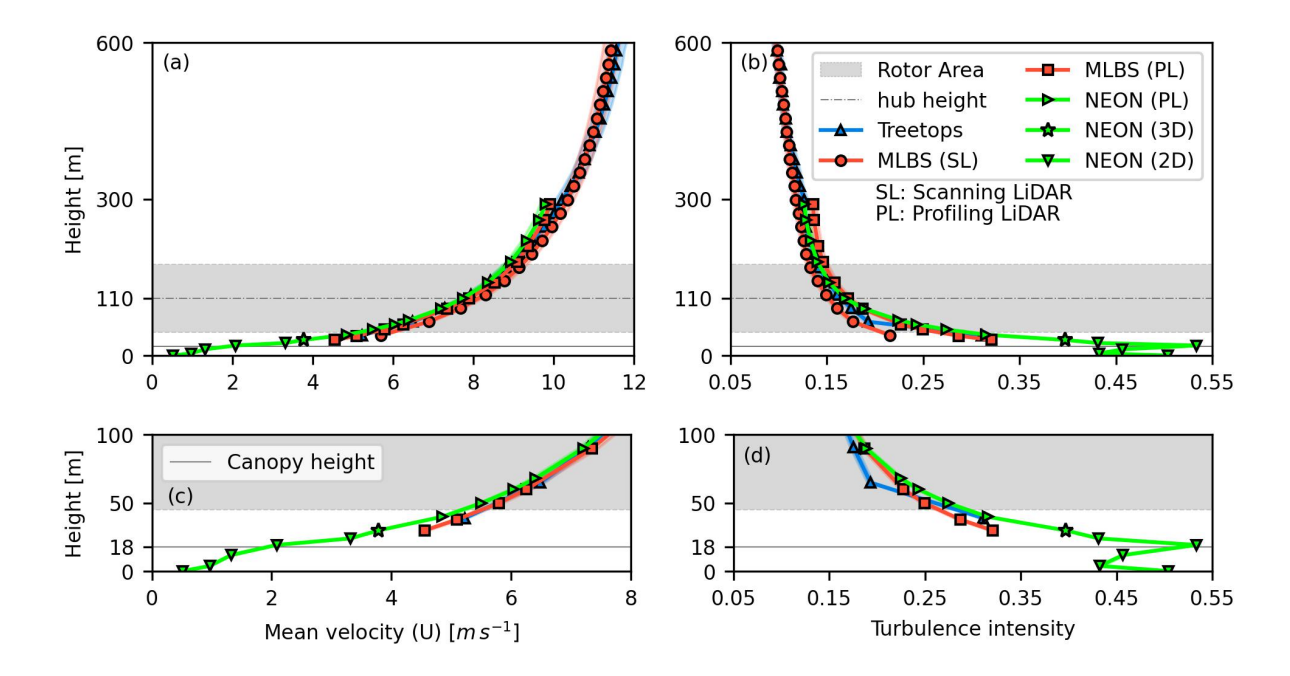


Figure 8. Vertical profiles of (a) mean wind speed and (b) turbulence intensity (TI). Plots (c) and (d) report the mean wind speed and TI profiles, respectively, below 100 m above ground.

below 100 m (Fig. 8d). Above 100 m no difference among mean wind speed or TI profiles is observed between sites (Fig. 8b), with the TI monotonically decreasing throughout the above-canopy interval.

Recalling that MLBS and Treetops are located within clearing areas, while the NEON site is within the forest canopy, the observed differences in wind speed and TI are likely due in part to the lower canopy roughness at MLBS and Treetops. This hypothesis is verified by calibrating the shear exponent (α) and displacement height (d) of Eq. (8) onto each 10-minute velocity profile for heights below the turbine's top tip (175 m). The results, in terms of mean values and standard deviation of d and α, are reported in Table 5. MLBS and Treetops feature very similar displacement heights (d = 9.7 m and 10 m on average), whereas NEON is characterized by a higher d (12.3 m) reflecting the higher tree density at that site, and the subsequent lower wind speed observed in Fig. 8c. Site-to-site differences are also reflected in the shear exponent, with NEON featuring the highest value (α = 0.31) due to the increased drag exerted by the denser canopy layer.

After assuming the IEA 3.4 MW wind turbine as reference, the 10-minute mean wind speed within the rotor area is utilized to predict the available power by calculating the capacity factor (CF) at each site. The CF is calculated based either on the hub-height wind speed (U_{hub}) or the rotor equivalent wind speed (Eq. 6) as input to the power curve. The CF (reported in Table 5) is above 50% on average for each site, consistent with relatively high average wind speed ($7.63 \, \text{m s}^{-1}$ to $8.13 \, \text{m s}^{-1}$).

Smaller CF values are obtained at MLBS and NEON (with respect to Treetops) based on the rotor-averaged wind speed, which confirms the role played by the shear generated at the canopy top in reducing the wind resources even for tall wind



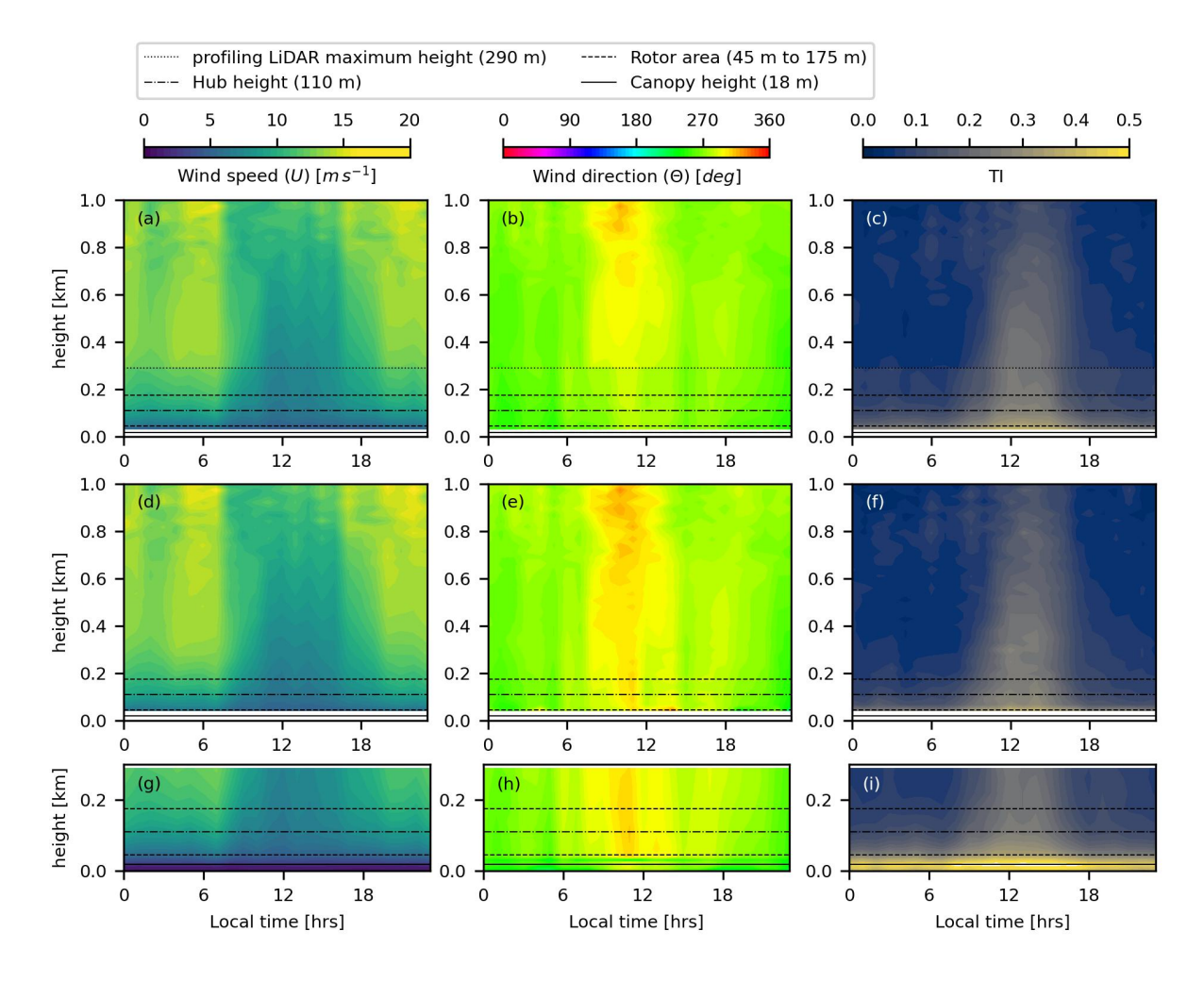


Figure 9. Daily averages of (a, d, g) wind speed, (b, e, h) wind direction and (c, f, i) turbulence intensity obtained from September 2024 through March 2025. Plots (a-c) refer to the MLBS site, plots (d-f) to Treetops and (g-i) to the NEON site.

turbines. The NEON site is characterized by the lowest hub-height and equivalent wind speed values, as well as the lowest predicted capacity factor (52.9% vs. ≥ 54% at the other sites) (Table 5). The present results demonstrate that, even for tall wind turbines featuring hub-height 5.5 times taller than the forest layer, the local canopy roughness is still a crucial parameter impacting the available wind resource. A more robust verification on canopy influence would require wind measurements over a nearby site that had zero forest canopy influence; we note that the small clearing sizes at MLBS and Treetops excluded this.

4.1.2 Diurnal variability

320 After assessing the overall wind resources at the tested sites, their diurnal variability is investigated. Based on the quality-controlled wind components resolved by each Lidar, the wind statistics are visualized in Fig. 9 as diurnal averages of wind



330



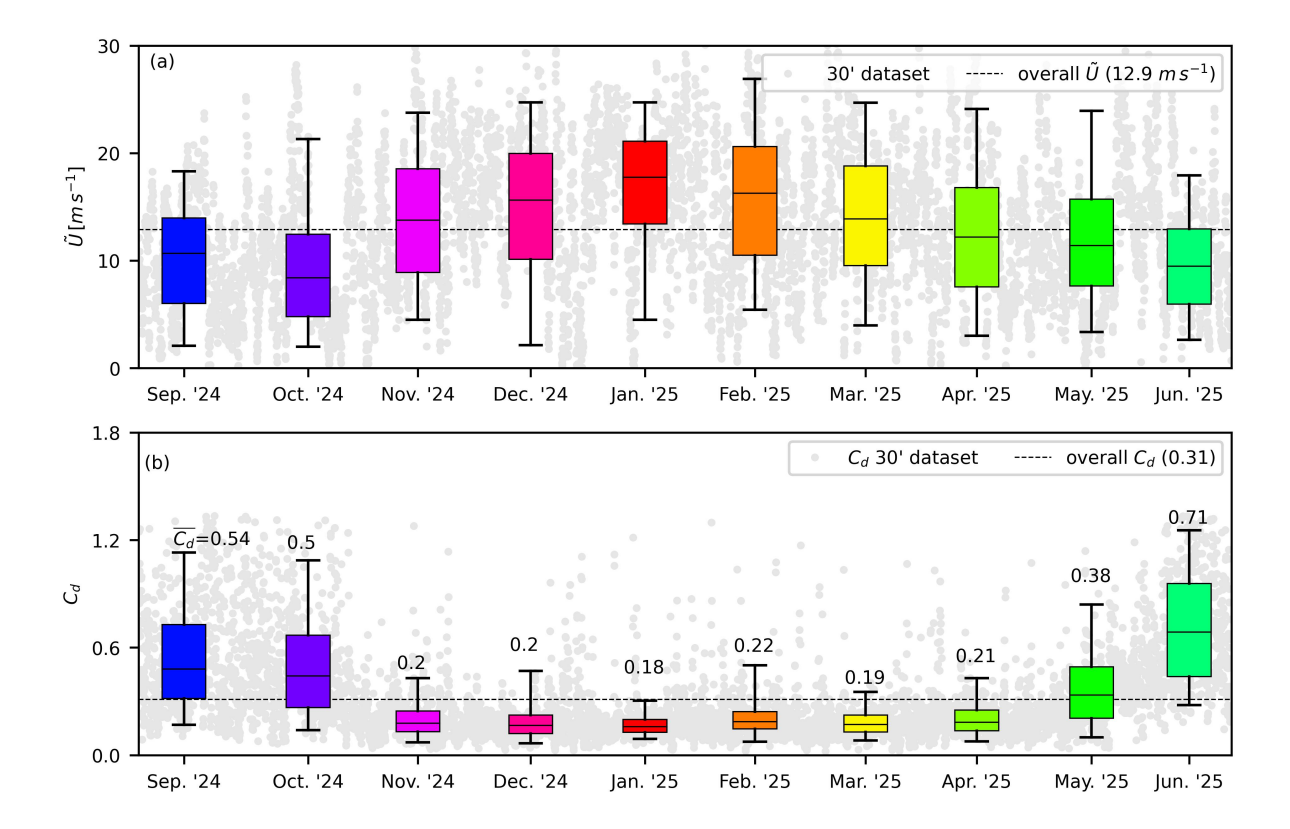


Figure 10. Quantification of wind variability across months at the NEON site. (a) Mean wind speed every 30 minutes probed at 1 km height; the whisker plots report the monthly statistics. (b) Drag coefficient time series and monthly statistics; the numbers report the average C_d for each month.

speed (Fig. 9a, d and g), wind direction (Fig. 9b, e and h) and TI (Fig. 9c, f and i). These statistics are based on 30-minute datasets collected within the same hour and then averaged together. For all the tested sites, the daily averages of wind speed and TI exhibit diurnal variability consistent with classical ABL flows above the surface layer, namely stronger wind and lower TI during the night (due to negative buoyancy fluxes) shifting to lower wind and higher TI during the day (due to the onset of a positive buoyancy flux). This scenario has also been corroborated over a deciduous forest in the Appalachian mountains by a recent experimental campaign based on long-term Lidar measurements (Lee et al., 2025).

The synergistic use of meteorological tower and profiling Lidar at the NEON site (Fig. 9g-i) allows us to capture the transition from constantly low wind speed and high TI below the canopy to the more classical ABL flow above the canopy. Finally, the diurnal average of wind direction (Θ) at all sites reveals West-North-West ($\Theta=300^\circ$) flow during the day and Westerly ($\Theta=270^\circ$) flow during the night throughout the above-canopy layer, consistent with the wind rose extracted from the 3D sonic anemometer during previous years (Fig. 2b).





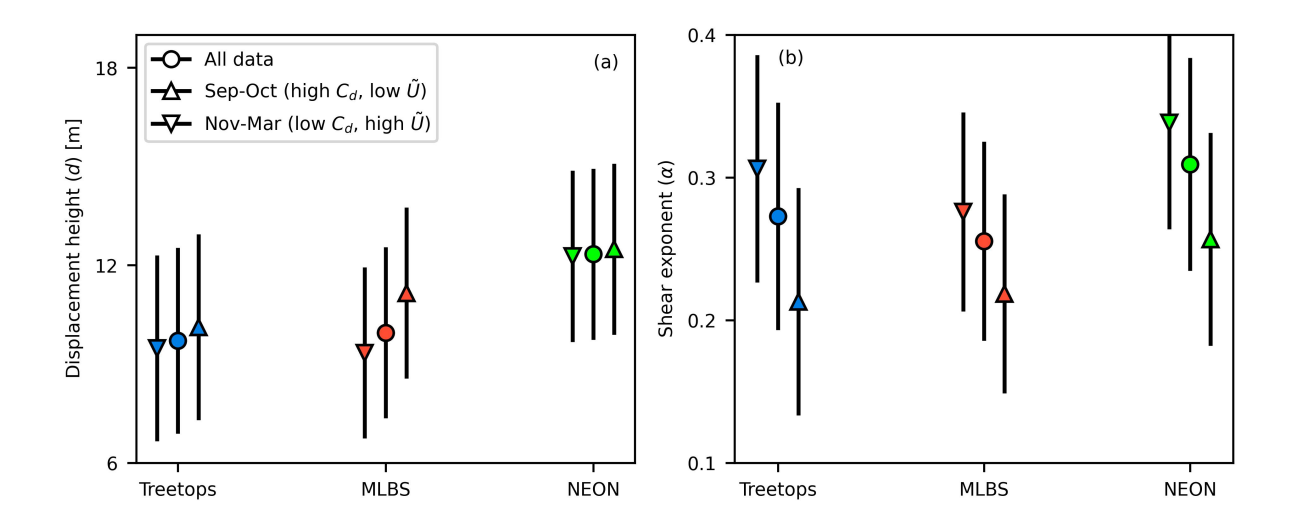


Figure 11. Statistics of mean velocity parameters (d, α) calculated for high C_d /low \tilde{U} -months (September-October) and low C_d /high \tilde{U} -months (November-March), respectively. (a) Displacement height, d. (b) Shear exponent, α . Symbols refer to mean values, while the uncertainty intervals report the standard deviation.

4.1.3 Monthly variability

335

340

345

350

From the analysis of annual wind data collected at NEON by the 3D sonic anemometer (Fig. 2), the annual senescence cycle occurring along the Appalachian forests (Fig. 3) modulates the wind speed in the above-canopy layer by changing the momentum absorption (and thus the C_d) on a monthly time scale. Additionally, the low synoptic wind speed during Summer and higher wind speed during Fall-Spring in the U.S. Southeast (quantified by \tilde{U}) are expected to modulate the wind resources above the canopy.

The monthly averaged statistics of \tilde{U} and C_d (reported in Fig. 10a and b, respectively, by box plots) show two distinct periods within the month-to-month transition. The first period (November-April) is characterized by \tilde{U} above the average (due to strong synoptic wind conditions in the U.S. Southeast) and low canopy drag ($C_d \leq 0.22$ on average) due to the absence of leaves. The second period (September-October and May-June), in contrast, features low \tilde{U} due to weaker synoptic wind and high C_d (≥ 0.5 on average) due to the higher foliage density within the canopy.

The wind speed within the rotor area is expected to be influenced by the variations of C_d and \tilde{U} . To address this point, the mean wind speed parameters (d, α) , previously calibrated at each site for each 30-minute dataset, are now averaged separately during either November-March or September-October. The period April-June is not considered here since the full Lidar data are unavailable from MLBS and Treetops. The result, plotted in Fig. 11, indicates lower displacement height (9.5 m, 9.3 m) and 12.3 m at Treetops, MLBS and NEON, respectively) during November-March due to the lower momentum absorption from the canopy (Fig. 11a). In contrast, the higher drag coefficient induced by the forest canopy from September through October results in higher values of d, i.e. 10.1 m, 11.2 and 12.5 m at Treetops, MLBS and NEON, respectively (Fig. 11a). The shear



360

365



exponent, α , follows the opposite trend (Fig. 11b). The stronger synoptic wind occurring during November-March induces higher shear in the above-canopy velocity profiles, which results in higher averaged α values (0.31, 0.28 and 0.34 at Treetops, MLBS and NEON, respectively). Conversely, the weaker synoptic wind speeds occurring during September-October result in lower shear ($\alpha = 0.21, 0.22$ and 0.26 averaged at Treetops, MLBS and NEON, respectively). This result further corroborates the hypothesis that changes in the canopy roughness affect the mean wind speed even for the tall wind turbine assumed as model in this work.

4.2 Correlation of the wind resources with C_d and $ilde{U}$

In the previous Subsection, the quantitative differences in the mean wind speed parameters (d and α) between the November-March and September-October months have been linked to the variations of C_d and \tilde{U} within these periods which, in turn, are caused by the annual senescence and synoptic wind transitions, respectively. The wind speed profile within the rotor layer is therefore determined both by the momentum entrainment from the upper ABL and the momentum absorption from the canopy. Here, we extend the analysis to establish which of these two factors is more correlated with the wind resources within the rotor layer. For each month of data, the correlation coefficient $\rho[x,y]$ is evaluated at each measured height assuming either $x=C_d$ or $x=\tilde{U}$ and y=U(z), $\mathrm{TI}(z)$ and $U^3(z)$, respectively. The analysis is based on data collected at the NEON site by the profiling Lidar and the 2D and 3D sonic anemometers, since NEON is the only site featuring 10 months of data collection below and above the canopy.

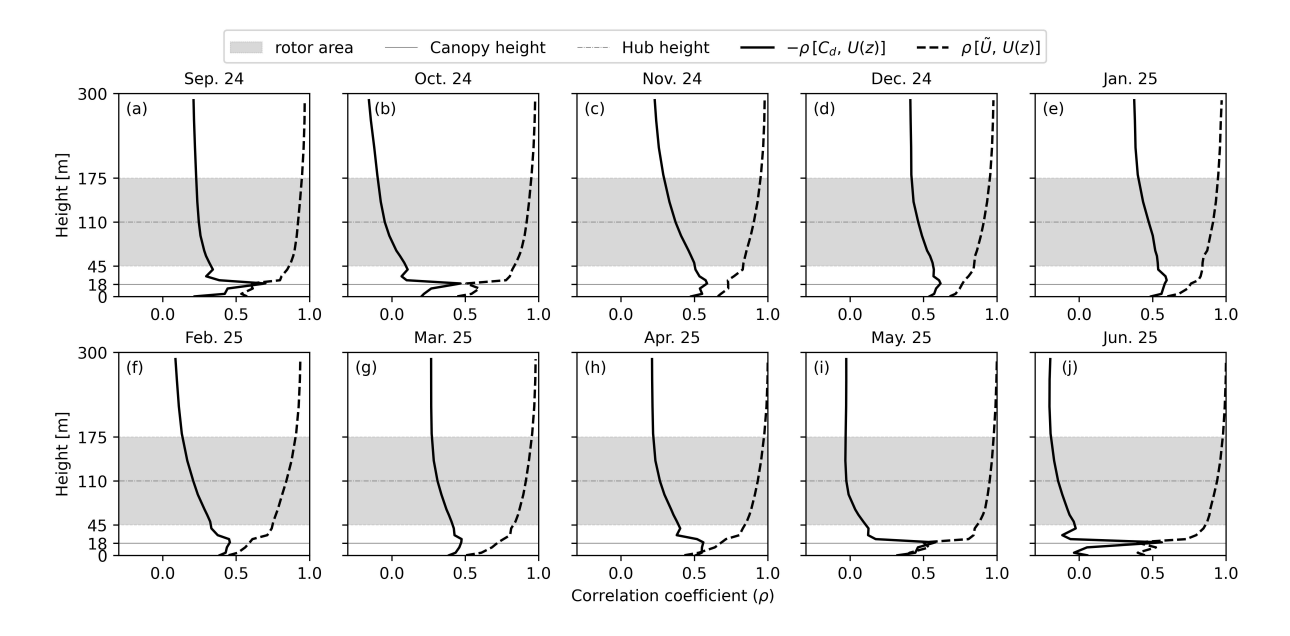


Figure 12. Correlation profiles of mean wind speed vs. drag coefficient ($\rho[C_d, U]$, continuous lines) and TI vs. \tilde{U} ($\rho[\tilde{U}, U]$, dashed lines) for each month at the NEON site.





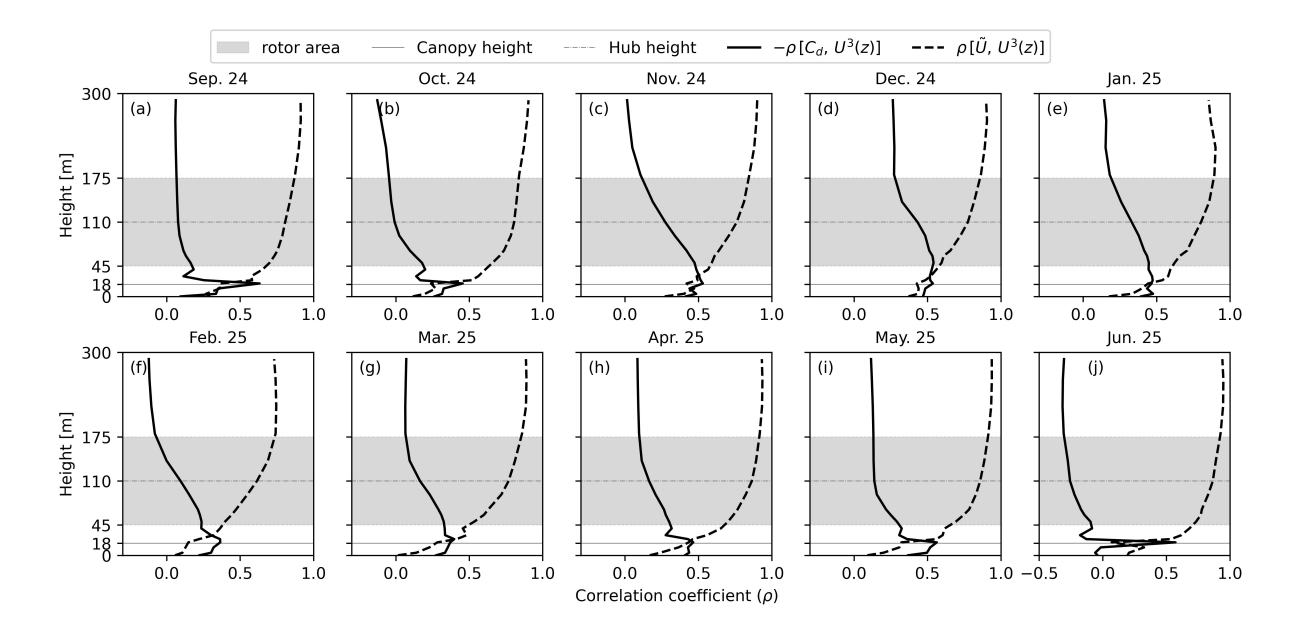


Figure 13. Correlation profiles of predicted power in region II ($\propto U^3$) vs. drag coefficient ($\rho[C_d, U^3]$, continuous lines) and TI vs. \tilde{U} ($\rho[\tilde{U}, U^3]$, dashed lines) for each month at the NEON site.

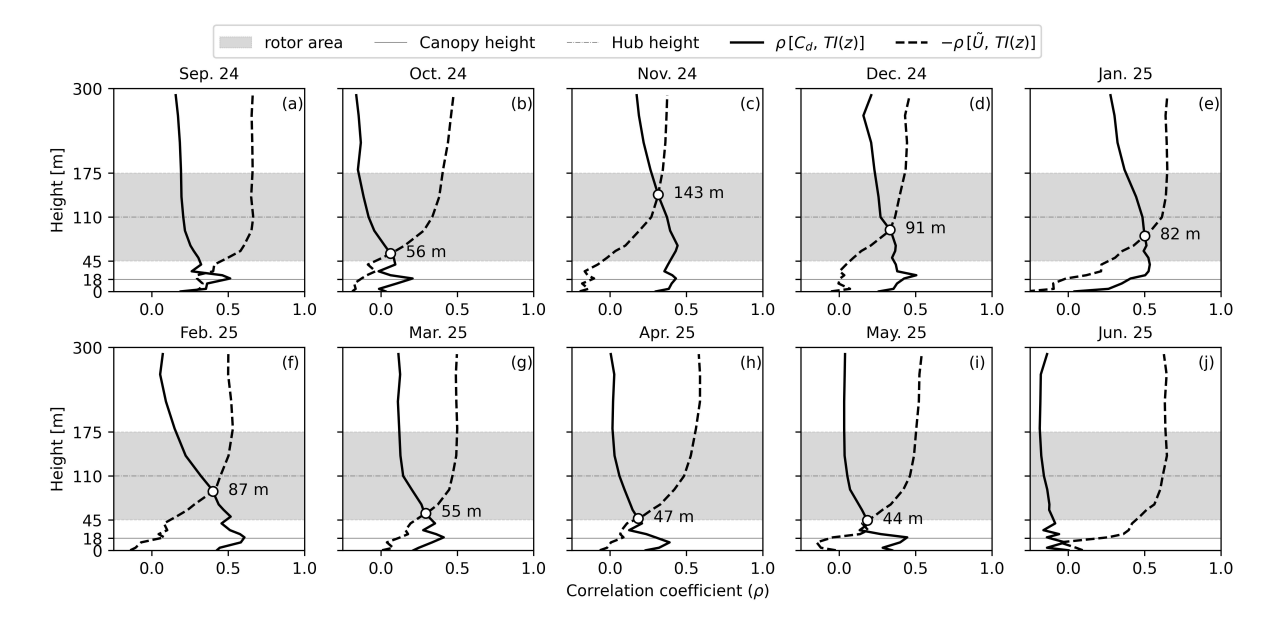


Figure 14. Correlation profiles of TI vs. drag coefficient ($\rho[C_d, \text{TI}]$, continuous lines) and TI vs. \tilde{U} ($\rho[\tilde{U}, \text{TI}]$, dashed lines) for each month at the NEON site. For panels (b)-(i), the circle symbols report the height of intersection between the two correlation profiles.



370

375

380

385

390

395

400



The correlation profiles $\rho[U(z),C_d]$ and $\rho[U(z),\tilde{U}]$ are reported in Fig. 12 and 13 for each month of data. It is observed that, throughout the months, the wind speed always exhibits larger correlation with the upper ABL velocity ($\rho[U(z),\tilde{U}] \geq 0.8$) than the drag coefficient ($-0.5 < \rho[U(z),C_d] < 0$). This is expected since the effect of the canopy roughness is typically limited to 5 to 6 times the canopy height (90 m to 108 m) (Finnigan et al., 2009), i.e. below the hub height (110 m). Thus, the correlation between the local wind speed and the canopy roughness reaches a maximum near the canopy top, while the correlation between the local wind speed and the velocity in the upper ABL increases with height. Similarly, from Fig. 13, the predicted power in region II (here approximated by U^3) shows limited correlation with C_d ($-0.5 < \rho[U^3(z), C_d] < 0$) and higher correlation with \tilde{U} within the rotor area ($0.5 \le \rho[U^3(z), \tilde{U}] \le 0.9$). For tall wind turbines, therefore, the available power within selected rotor height intervals (2.5h to 9.7h) is mainly correlated to the momentum entrainment from the ABL top and only marginally correlated to the canopy roughness.

The correlation profiles of TI against C_d and \tilde{U} ($\rho[C_d, \text{TI}]$ and $-\rho[\tilde{U}, \text{TI}]$) (Fig. 14) show a different trend than those for U and U^3 . From October 2024 through May 2025, the $\rho[C_d, \text{TI}]$ and $-\rho[\tilde{U}, \text{TI}]$ profiles are similar in magnitude and intersect within the rotor area, with $\rho[C_d, \text{TI}] > -\rho[\tilde{U}, \text{TI}]$ below the intersection height. This intersection reaches a maximum located in the top half of the rotor layer (143 m) in November, indicating that for the majority of the rotor layer, the TI is more correlated with the canopy roughness than the wind conditions in the free atmosphere. From November until April, the correlation between TI and \tilde{U} becomes more prominent, while $\rho[C_d, \text{TI}]$ is nearly constant. Finally, during the period May-June (characterized by higher C_d), $\rho[C_d, \text{TI}]$ decreases. Therefore, we conclude that months characterized by lower C_d feature higher correlation between C_d and TI, as opposed to months characterized by high C_d . This result, which might seem counterintuitive, is related to the correlation between C_d and $\overline{u'u'}$, and is discussed further in Appendix A. Overall, our analysis indicates that even for tall wind turbines (rotor heights between 2.5 to 9.7 times the canopy height), TI values within the rotor layer are similarly correlated to both the canopy roughness and wind conditions in the upper ABL.

4.3 Spatial heterogeneity of the flow statistics

After quantifying the influence of canopy and upper ABL velocity on the wind resources at the NEON site, we focus on the spatial heterogeneity across the three tested sites. This aspect is crucial for wind resource assessment over fragmented canopies and complex terrain. From the perspective of the optimization of a wind farm layout, the wake evolution downstream of wind turbine arrays is determined, among various factors, by the incoming flow inhomogeneities (see, for example, Nygaard et al., 2022; Lanzilao and Meyers, 2022), hence its quantification for a real-flow scenario is instrumental to the development of the next generation of wind turbines. Additionally, from a numerical simulation perspective, the spatial heterogeneity is a key factor influencing the required grid resolution (Lundquist et al., 2012; Wiersema et al., 2020; Solbakken et al., 2021; Wise et al., 2021) and the choice of turbulence closure scheme (Juliano et al., 2022).

The quantification of the vertical extent (i.e., altitude) of heterogeneity is addressed by the two-sample Kolmogorov-Smirnov (KS) test of statistical significance (Pratt and Gibbons, 1981). Given two sets of samples representing two random processes, the KS test quantifies the probability (p) that the null hypothesis (i.e., the two samples are extracted from the same PDF) is true. For probabilities lower than a chosen significance level (typically assumed p = 0.05), the null hypothesis is rejected (i.e., the



410



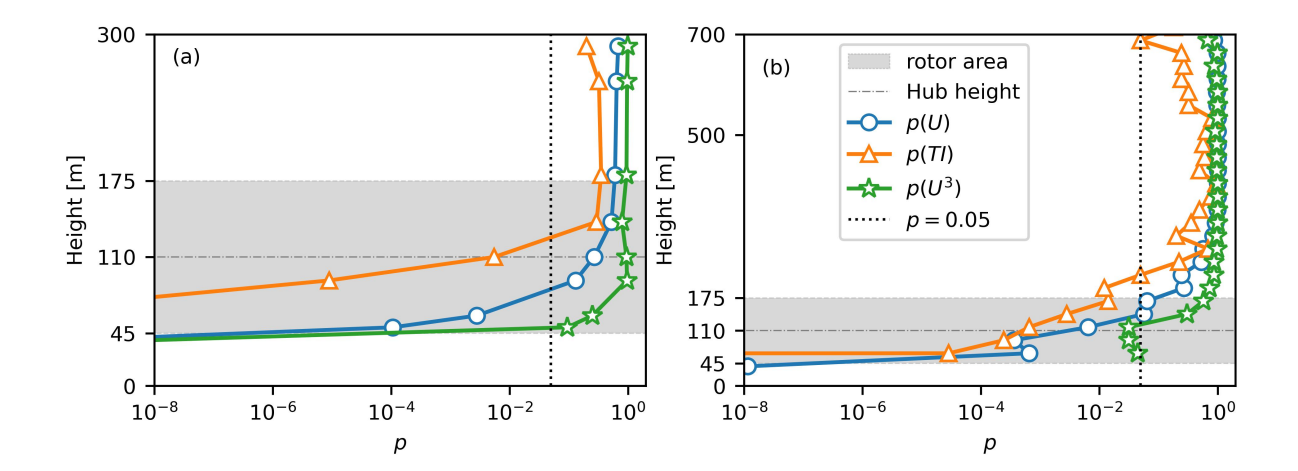


Figure 15. Kolmogorov-Smirnov test of statistical significance between wind speed, TI and U^3 (assumed as a proxy of power in region II) sampled at different sites. (a) NEON vs. MLBS (profiling Lidar). (b) MLBS vs. Treetops (scanning Lidar).

Table 6. Maximum height featuring spatially heterogeneous wind statistics based on the Kolmogorov-Smirnov test.

Quantity	NEON – MLBS	MLBS – Treetops
Wind speed	71 m	140 m
Power	50 m	119 m
TI	116 m	221 m

samples are extracted from different PDFs), whereas for p > 0.05 no statistical difference is found between the two samples. For the present work, the KS test is adopted to quantify statistical differences both between the NEON and MLBS sites (based on profiling Lidar data) and between the MLBS and Treetops sites (based on scanning Lidar data) at common heights.

The vertical profiles of KS probability (p) are reported in Fig. 15. Between NEON and MLBS (Fig. 15a), statistically significant differences are found within the rotor layer (gray shaded area), with the TI featuring the largest vertical extent of heterogeneity $(p < 0.05 \text{ for } z \le 110 \text{ m})$, i.e. below hub height) followed by U and U^3 . Similarly, the comparison between MLBS and Treetops (Fig. 15b) reveals inhomogeneities in the U and TI profiles for the entire rotor area, while site differences in U^3 are found only for the bottom half of the rotor area. The height where p crosses the critical value for each quantity is estimated through a linear interpolation of the distributions shown in Fig. 15 and reported in Table 6. Both for U and TI, the maximum heights where site differences are present are located well within the rotor layer $(45 \text{ m} \le z \le 175 \text{ m})$ or above it. For U^3 the vertical extent of heterogeneity falls near the bottom of the rotor layer when the NEON and MLBS sites are compared, and it exceeds the hub height when comparing Treetops and MLBS.

In analogy to the monthly variations of C_d and \tilde{U} (Fig. 10) and the subsequent correlation with the wind resources (Fig. 12, 13 and 14), the site heterogeneity is also expected to vary across months. Thus, for the 7 months of the LEAFF campaign when



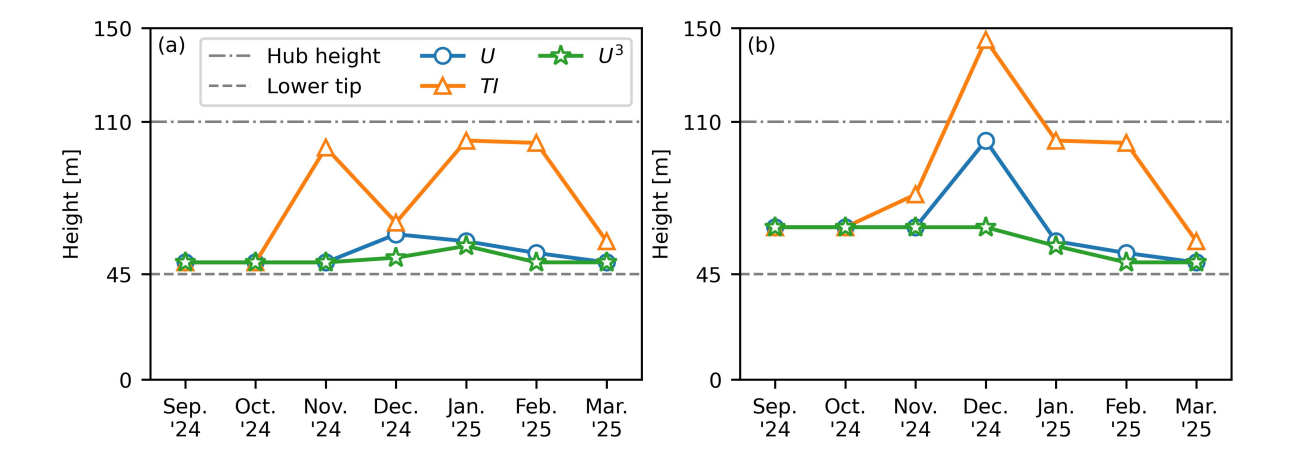


Figure 16. Maximum height featuring statistically significant differences between sites based on the two-sample Kolmogorov-Smirnov test. (a) MLBS vs. NEON site (profiling Lidar data). (b) MLBS vs. Treetops (scanning Lidar data).

all the Lidars are available (i.e. September 2024 through March 2025), the heterogeneity of the wind resources is quantified by the Kolmogorov-Smirnov test applied individually to each month of data. The height where the Kolmogorov-Smirnov probability (*p*) crosses 0.05, i.e. the maximum height where site inhomogeneities are found, is evaluated for each month and reported in Fig. 16a for NEON vs. MLBS data (collected by the profiling Lidars) and in Fig. 16b for MLBS vs. Treetops data (collected by the scanning Lidars).

It is observed that, during the months of highest wind conditions and lowest C_d (i.e. November through February), all the wind statistics show enhanced heterogeneity with respect to the overall values quantified in Table 6. Specifically, the TI features the highest degree of site heterogeneity, with maximum vertical extents reaching between 50 m and 175 m, i.e. into the rotor area, for the entire duration of the campaign. In contrast, U and U^3 inhomogeneities reach only into the lowest portion of the rotor area. Thus, in addition to low C_d , the months featuring stronger synoptic wind conditions (November through March) also feature enhanced site heterogeneity.

5 Conclusions

430

In this study, data from a novel experimental campaign are used to quantify wind resources in a forested region of the U.S. Southeast. Our analysis focuses on tall turbines (with hub heights of $100\,\mathrm{m}$ or greater), which are likely to experience higher wind speeds due to increased separation between the canopy drag layer and the rotor layer. Three sites, spaced $\leq 1.6\,\mathrm{km}$ apart and located in the Appalachian mountains, are investigated from September 2024 through June 2025. One site is immersed in a $18\,\mathrm{m}$ -tall deciduous forest and the other two are in small clearings surrounded by the same forest type. The sites are equipped with four Doppler wind Lidars (two profiling and two scanning Lidars) to probe the above-canopy wind speed, while below-canopy wind data are collected by the NEON flux tower equipped with 2D and 3D sonic anemometers.



435

440

445

450

455



The wind statistics examined in this work are the horizontal wind speed (U), the turbulence intensity (TI) and U^3 within region II of a suitable tall wind turbine model (IEA 3.4 MW wind turbine, featuring rotor area between 45 m and 175 m), assumed as an approximation of the power. The availability of these statistics from the ground up to 1 km height allows: 1) quantifying the month-to-month variation of the two main phenomena affecting the flow momentum, i.e. momentum absorption by the canopy layer (quantified by the drag coefficient, C_d) and momentum entrainment from the free atmosphere (quantified by the wind speed at 1 km above ground, \tilde{U}); 2) quantifying the correlation of C_d and \tilde{U} with the wind statistics in the rotor layer; and 3) quantifying the spatial heterogeneity of the wind resources across the sites.

After assessing the available wind resources (capacity factors between 52% and 55%) the following conclusions are made:

- The site characterized by the highest canopy drag exhibited the lowest capacity factor (-1.5% to -1% with respect to the other two sites) and the highest shear exponent (0.34 versus 0.27 to 0.33). This indicates that, even for tall wind turbines (hub height of 110 m), the local canopy roughness is still a relevant parameter. For all the tested sites, higher (lower) displacement heights are found for months characterized by high (low) C_d . Similarly, larger (smaller) shear exponent values are found for higher (lower) values of \tilde{U} . These results highlight the competing effects of canopy drag and wind synoptic conditions on the mean velocity profile within the rotor area.
- After establishing the effect of both canopy drag and synoptic wind conditions on the wind resources, we perform a correlation analysis with C_d and \tilde{U} for each month at the forested site. Low correlation coefficient ($\rho \leq 0.5$) is found between C_d and mean wind speed within the rotor area, as well as between C_d and U^3 in region II. These quantities are more strongly correlated with the wind in the upper ABL (correlation coefficients above 0.5). The TI, in contrast, shows similar correlation both with \tilde{U} and C_d (ρ between -0.25 and 0.6).
- The site heterogeneity, quantified by the Kolmogorov-Smirnov test, is more prominent for the TI (reaching up to $221 \,\mathrm{m}$ above ground), followed by the wind speed (up to $141 \,\mathrm{m}$) and U^3 (up to $41 \,\mathrm{m}$). Thus, site-related inhomogeneities still affect the wind resources even within the rotor layer of tall turbines (i.e. $45 \,\mathrm{m}$ to $175 \,\mathrm{m}$). When the analysis is carried out separately for each month, site inhomogeneities are found to be more pronounced during the months of higher wind speed and lower canopy drag (November through March), with statistically significant differences reaching well into the rotor area (i.e. between $45 \,\mathrm{m}$ and $150 \,\mathrm{m}$) for all the statistical quantities.

The present work provides insights about the location of wind measurements in order to accurately estimate wind energy resources in forested regions. While deploying a Lidar in a clearing is less expensive and logistically easier, this location may not capture the full extent of TI that a rotor disk would encounter and may not resolve the TI variability induced by a high-density forest canopy. On the other hand, utilizing one Lidar to connect the below-canopy velocity profile (measured by tower-based sonic anemometers) with the above-canopy flow is more expensive and requires merging observations recorded by different instruments, thus with different statistical accuracy and resolution. Ultimately, the measurement location could affect the estimated power production and the estimated fatigue loads on turbine blades, which are primarily determined by the TI (IEC, 2019). The present work emphasizes that the wind resource heterogeneity arising over fragmented forest cover and terrain cannot be neglected even for tall wind turbines, thus making it beneficial to probe multiple locations.



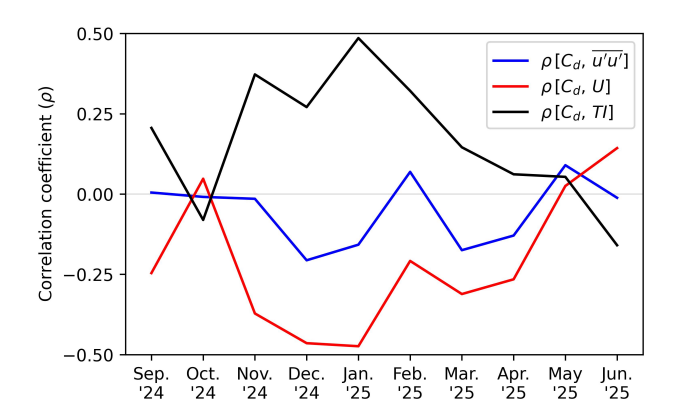


Figure A1. Correlation coefficients of C_d vs. $U, \overline{u'u'}$ and TI at hub height for each month.

Overall, the present findings address some of the long-standing challenges of wind resource assessment in forested areas, notably how seasonal variability and site heterogeneity affect wind statistics. These results are important for wind farm siting, as the spatio-temporal extent of site-related heterogeneity is a key aspect of wind farm performance. Additionally, the present observations can be used to validate mesoscale and LES models that include canopy parameterizations, with a focus on capturing variations in winds and turbulence due to modeled canopy processes.

Data availability.

470

The scanning and profiling Lidar data are available at the Wind Data Hub - Tall Turbines Project website (wdh.energy.gov/data/ttp).

475 The Lidar data shown in this work are saved in the following metadata channels:

- NEON tower profiling Lidar: https://wdh.energy.gov/ds/ttp/mlbs.lidar.z01.00
- MLBS profiling Lidar: https://wdh.energy.gov/ds/ttp/mlbs.lidar.z02.00
- MLBS scanning Lidar: https://wdh.energy.gov/ds/ttp/mlbs.lidar.z03.c0
- Treetops scanning Lidar: https://wdh.energy.gov/ds/ttp/mlbs.lidar.z04.c0
- The data collected by the NEON meteorological tower (NEON, 2025a, b) are publicly available on the NEON website.

Appendix A: Analysis of the correlation between TI and drag coefficient

In Fig. 14, it is observed that, for heights within the modeled rotor area ($45 \,\mathrm{m}$ to $175 \,\mathrm{m}$) the TI is more correlated with the drag coefficient than the upper ABL velocity. This situation is more prominent for months characterized by lower values of C_d , i.e. November through April. The higher correlation between TI and C_d in presence of relatively low C_d values might seem





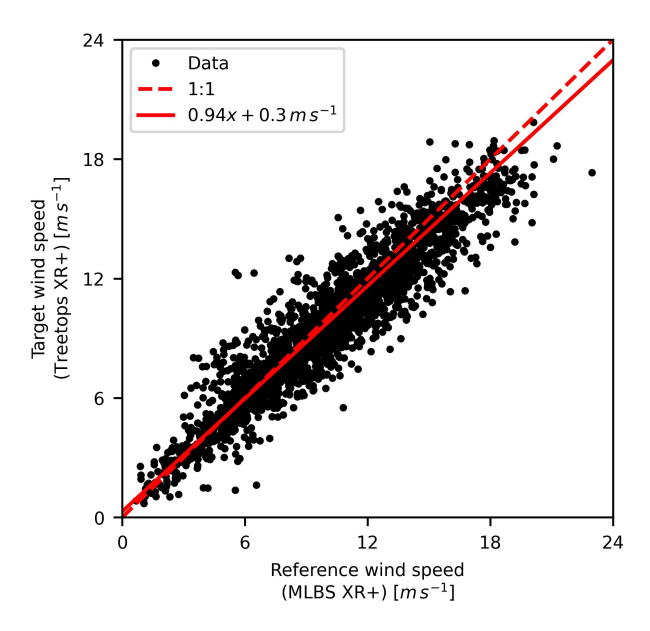


Figure A1. Variance ratio method applied to the mean velocity between reference scanning Lidar data (collected at MLBS) and target data (collected at Treetops), both of them recorded at 117 m above ground.

a counterintuitive result, which is further explored here. The observed trend of ρ[C_d, TI] can be explained recalling that, for each height: TI = (ū'ū'/U²)^{0.5} (Eq. 5), hence the correlation between TI and C_d can be explained in terms of the correlation between C_d and ū'ū (ρ[C_d, ū'ū']) and the correlation between C_d and U (ρ[C_d, U]). These two quantities are calculated for each month at hub height and reported in Fig. A1. Here it is observed that the correlation between C_d and ū'ū' always assumes relatively low values (between -0.2 and 0.1), thus ρ[C_d, TI] is primarily determined by the correlation between C_d and U.
The months characterized by high C_d (i.e. September, October, May and June) feature lower values of ρ[C_d, U] (±0.2). This is due to the enhanced turbulent mixing (induced by higher wind speed) which reduces the correlation between C_d (at z = h, i.e. 18 m) and the hub-height wind speed (at 110 m). This, in turn, reduces the correlation between C_d and TI, thus explaining the lower intersection values observed in Fig. 14b and 14i. By contrast, the months characterized by lower leaf coverage, and therefore lower C_d (i.e. November through April), are characterized by lower vertical turbulent mixing arising from the canopy top which increases the correlation between the C_d and the hub-height wind speed and, in turn, increases the correlation between C_d and TI.

Appendix B: The Measure Correlate Predict algorithm

500

The Measure Correlate Predict (MCP) algorithm is a method to predict the wind resources at a target site based on the knowledge of the wind resources at a reference site located within kilometers from the target. When a certain wind statistic is simultaneously available at both sites, a linear regression is established between them. When the data are missing from the



515

520



target site, the slope and intercept calibrated from the linear regression are used to fill the data gaps using the reference site data as input.

Several methods have been examined by Rogers et al. (2005) in the context of onshore wind resource prediction to establish which algorithm returns the less statistically biased resources at the target site. Among the various MCP methods, Rogers et al. (2005) showed that the best one (returning unbiased estimates of the mean wind speed, mean wind direction, predicted power and wind speed distribution at the target site) is the variance ratio method. The latter assumes a time series, y(t), sampled at the target site characterized by a certain mean (μ_T) and standard deviation (σ_T) , and a simultaneous time series, x(t), sampled at the reference site characterized by another mean (μ_R) and standard deviation (σ_R) . The predicted time series $(\hat{y}(t))$ at the target site is estimated according to the variance ratio method as (Rogers et al., 2005):

510
$$\hat{y}(t) = \frac{\sigma_T}{\sigma_R} x(t) + \mu_T - \frac{\sigma_T}{\sigma_R} \mu_R.$$
 (A1)

It is noticed that Equation A1 returns unbiased estimates of the mean and standard deviation of y since: $\hat{y} = \overline{y} = \mu_T$ and $\sigma(\hat{y}) = \sigma(y) = \sigma_T$. Thus, the statistics calculated at the target site are not affected by the MCP algorithm.

As reported in Section 2.2, the scanning Doppler Lidar data collected at Treetops feature significantly larger temporal gaps than the other two sites, mainly due to several power outages reducing the data availability within the height interval of interest (see Fig. 4). On the other hand, the scanning Doppler Lidar at the MLBS site shows almost no data gap. Thus, for each height scanned by the two instruments, the data collected at MLBS and those collected at Treetops are utilized as reference and target of the MCP variance ratio method, respectively. The quantities estimated through the MCP algorithm at Treetops are the 30-minute average wind speed, wind direction and TI. As an example of the MCP regression analysis, the comparison between 30-minute average wind speed collected by the two scanning Lidars at 117 m height (i.e. the value closest to the reference turbine's hub-height, 110 m) is reported in Fig. A1. The mean and standard deviation at the target and reference sites return 0.94 and 0.30 m s⁻¹ as slope and intercept values, respectively. Thus, for temporal periods where the Lidar measurements at Treetops are not available, the reference data (simultaneously collected at MLBS) are injected in the linear model to predict the statistic at the target site (Treetops).

Author contributions. MP, SW, SDW contributed to sensor deployment, conceptualization, data collection and analysis. RSA, TL, YL, SF,
 KP, RR, LB and JF provided feedback and supervised the work. JF acquired funding and is the Principal Investigator of the project. MP wrote the original manuscript.

Competing interests. The authors declare no competing interests.

Acknowledgements. The authors greatly thank the staff at MLBS, Mountain Lake Lodge, and NEON for making this campaign possible and for ensuring power availability. We especially acknowledge the assistance of Jaime BeVille Jones (MLBS Station Manager), Eric Nagy





530 (MLBS Associate Director), Heidi Stone (Mountain Lake Lodge) and Rommel Zulueta, Bill Martin, and the site technicians at NEON. This research was supported by the Wind Energy Technologies Office within the Office of Energy Efficiency and Renewable Energy of the U.S. Department of Energy. For M.P., R.S.A., T.L. and S.W., this work was performed under the auspices of the U.S. Department of Energy by Lawrence Livermore National Laboratory under Contract DE-AC52-07NA27344 with release number LLNL-JRNL-2010900. For Y.L., S.F., K.P., R.R., L.K.B., and J.D.F., work was performed at Pacific Northwest National Laboratory which is operated for DOE by Battelle Memorial Institute under Contract DE-A06-76RLO 1830. 535





References

- Ackermann, T. and Söder, L.: Wind energy technology and current status: a review, Renew. Sustain. Energy Rev., 4, 315–374, https://doi.org/10.1016/S1364-0321(00)00004-6, 2000.
- Aitken, M. L., Kosović, B., Mirocha, J. D., and Lundquist, J. K.: Large eddy simulation of wind turbine wake dynamics in the stable boundary layer using the Weather Research and Forecasting Model, J. Renew. Sustain. Ener., 6, https://doi.org/10.1063/1.4885111, 2014.
 - Al-Yahyai, S., Charabi, Y., and Gastli, A.: Review of the use of numerical weather prediction (NWP) models for wind energy assessment, Renew. Sustain. Energy Rev., 14, 3192–3198, https://doi.org/10.1016/j.rser.2010.07.001, 2010.
 - Archer, C. L., Wu, S., Ma, Y., and Jiménez, P. A.: Two corrections for turbulent kinetic energy generated by wind farms in the WRF model, Mon. Weather Rev., 148, 4823–4835, https://doi.org/10.1175/MWR-D-20-0097.1, 2020.
- Arnqvist, J., Segalini, A., Dellwik, E., and Bergström, H.: Wind statistics from a forested landscape, Bound.-Lay. Meteorol., 156, 53–71, https://doi.org/10.1007/s10546-015-0016-x, 2015.
 - Blankenhorn, V. and Resch, B.: Determination of suitable areas for the generation of wind energy in Germany: Potential areas of the present and future, ISPRS Int. J. Geo-Inf., 3, 942–967, https://doi.org/10.3390/ijgi3030942, 2014.
- Bortolotti, P., Tarres, H. C., Dykes, K., Merz, K., Sethuraman, L., Verelst, D., and Zahle, F.: IEA Wind Task 37 on Systems Engineering in Wind Energy WP2.1 Reference Wind Turbines, Tech. rep., International Energy Agency, https://www.nrel.gov/docs/fy19osti/73492.pdf, 2019.
 - Bunzel, K., Bovet, J., Thrän, D., and Eichhorn, M.: Hidden outlaws in the forest? A legal and spatial analysis of onshore wind energy in Germany, Energy Res. Social Sci., 55, 14–25, https://doi.org/10.1016/j.erss.2019.04.009, 2019.
- Butterworth, B. J., Desai, A. R., Townsend, P. A., Petty, G. W., Andresen, C. G., Bertram, T. H., Kruger, E. L., Mineau, J. K., Olson, E. R.,
 Paleri, S., et al.: Connecting land–atmosphere interactions to surface heterogeneity in CHEESEHEAD19, Bull. Am. Meteorol. Soc., 102,
 E421–E445, https://doi.org/10.1175/BAMS-D-19-0346.1, 2021.
 - Cescatti, A. and Marcolla, B.: Drag coefficient and turbulence intensity in conifer canopies, Agric. For. Meteorol., 121, 197–206, https://doi.org/10.1016/j.agrformet.2003.08.028, 2004.
- Chu, H., Christianson, D. S., Cheah, Y.-W., Pastorello, G., O'Brien, F., Geden, J., Ngo, S.-T., Hollowgrass, R., Leibowitz, K., Beekwilder,

 N. F., et al.: AmeriFlux BASE data pipeline to support network growth and data sharing, Sci. Data, 10, 614, https://doi.org/10.1038/s41597-023-02531-2, 2023.
 - Darwish, A. S. and Al-Dabbagh, R.: Wind energy state of the art: present and future technology advancements, Renew. Energy Environ. Sustain., 5, 7, https://doi.org/10.1051/rees/2020003, 2020.
- Eder, F., De Roo, F., Rotenberg, E., Yakir, D., Schmid, H. P., and Mauder, M.: Secondary circulations at a solitary forest surrounded by semi-arid shrubland and their impact on eddy-covariance measurements, Agric. For. Meteorol., 211, 115–127, https://doi.org/10.1016/j.agrformet.2015.06.001, 2015.
 - Finnigan, J. J., Shaw, R. H., and Patton, E. G.: Turbulence structure above a vegetation canopy, J. Fluid Mech., 637, 387–424, https://doi.org/10.1017/S0022112009990589, 2009.
- Fitch, A. C., Olson, J. B., Lundquist, J. K., Dudhia, J., Gupta, A. K., Michalakes, J., and Barstad, I.: Local and mesoscale impacts of wind farms as parameterized in a mesoscale NWP model, Mon. Weather Rev., 140, 3017–3038, https://doi.org/10.1175/MWR-D-11-00352.1, 2012.



580



- Fitch, A. C., Olson, J. B., and Lundquist, J. K.: Parameterization of wind farms in climate models, J. Climate, 26, 6439–6458, https://doi.org/10.1175/JCLI-D-12-00376.1, 2013.
- Foken, T., Göockede, M., Mauder, M., Mahrt, L., Amiro, B., and Munger, W.: Post-field data quality control, in: Handbook of micrometeorology: A guide for surface flux measurement and analysis, pp. 181–208, Springer, https://doi.org/10.1007/1-4020-2265-4_9, 2004.
 - García-Santiago, O., Hahmann, A. N., Badger, J., and Peña, A.: Evaluation of wind farm parameterizations in the WRF model under different atmospheric stability conditions with high-resolution wake simulations, Wind Energy Sci., 9, 963–979, https://doi.org/10.5194/wes-9-963-2024, 2024.
 - Gualtieri, G. and Secci, S.: Methods to extrapolate wind resource to the turbine hub height based on power law: A 1-h wind speed vs. Weibull distribution extrapolation comparison, Renewable Energy, 43, 183–200, https://doi.org/10.1016/j.renene.2011.12.022, 2012.
 - Hoen, B., Diffendorfer, J., Rand, J., Kramer, L., Garrity, C., and Hunt, H.: United States Wind Turbine Database, Tech. rep., U.S. Geological Survey, American Clean Power Association, and Lawrence Berkeley National Laboratory, https://doi.org/10.5066/F7TX3DN0, 2018.
 - IEC: Wind energy generation systems part 1: design requirements (Ed. 4), Tech. rep., International Electrotechnical Committee 61400-1, 2019.
- Juliano, T. W., Kosović, B., Jiménez, P. A., Eghdami, M., Haupt, S. E., and Martilli, A.: "Gray zone" simulations using a three-dimensional planetary boundary layer parameterization in the Weather Research and Forecasting Model, Mon. Weather Rev., 150, 1585–1619, https://doi.org/10.1175/MWR-D-21-0164.1, 2022.
 - Kane, B. and Smiley, E. T.: Drag coefficients and crown area estimation of red maple, Can. J. For. Res., 36, 1951–1958, https://doi.org/10.1139/x06-086, 2006.
- Konrad, C. E., Fuhrmann, C. M., Billiot, A., Keim, B. D., Kruk, M. C., Kunkel, K. E., Needham, H., Shafer, M., and Stevens, L.: Climate of the southeast USA: past, present, and future, in: Climate of the southeast United States: Variability, change, impacts, and vulnerability, pp. 8–42, Springer, https://doi.org/10.5822/978-1-61091-509-0_2, 2013.
 - Lalic, B., Mihailovic, D. T., Rajkovic, B., Arsenic, I. D., and Radlovic, D.: Wind profile within the forest canopy and in the transition layer above it, Environ. Modell. Software, 18, 943–950, https://doi.org/10.1016/S1364-8152(03)00068-9, 2003.
- Lanzilao, L. and Meyers, J.: A new wake-merging method for wind-farm power prediction in the presence of heterogeneous background velocity fields, Wind Energy, 25, 237–259, https://doi.org/10.1002/we.2669, 2022.
 - Lee, J. A., Doubrawa, P., Xue, L., Newman, A. J., Draxl, C., and Scott, G.: Wind resource assessment for Alaska's offshore regions: validation of a 14-year high-resolution WRF data set, Energies, 12, 2780, https://doi.org/10.3390/en12142780, 2019.
- Lee, T. R., Pal, S., Meyers, T. P., Krishnan, P., Saylor, R. D., and Heuer, M.: Vertical Structure of Turbulence in the

 Lower Atmospheric Boundary Layer above a Deciduous Forest in Complex Terrain, Agric. For. Meteorol., 373, 110745, https://doi.org/10.1016/j.agrformet.2025.110745, 2025.
 - Letizia, S., Robey, R., Bodini, N., Sanchez Gomez, M., Lundquist, J. K., Krishnamurthy, R., and Moriarty, P. J.: Tilted lidar profiling: Development and testing of a novel scanning strategy for inhomogeneous flows, J. Renewable Sustainable Energy, 16, https://doi.org/10.1063/5.0209729, 2024.
- Liu, Y., Feng, S., Berg, L. K., Wharton, S., Arthur, R., Turner, D. D., and Fast, J. D.: Benchmarking near surface winds in the HRRR analyses using multi-source observations over complex terrain in the southeastern United States, J. Appl. Meteorol. Climatol., 64, 1307–1322, https://doi.org/10.1175/JAMC-D-24-0163.1, 2025.
 - López-Martínez, F.: Are wind turbines integrated into landscape? an analysis of its social perception in a spanish mediterranean area, Landscape Ecol., 38, 3499–3515, https://doi.org/10.1007/s10980-023-01698-8, 2023.



640



- Lundquist, K. A., Chow, F. K., and Lundquist, J. K.: An immersed boundary method enabling large-eddy simulations of flow over complex terrain in the WRF model, Mon. Weather Rev., 140, 3936–3955, https://doi.org/10.1175/MWR-D-11-00311.1, 2012.
 - Ma, Y., Archer, C. L., and Vasel-Be-Hagh, A.: Comparison of individual versus ensemble wind farm parameterizations inclusive of sub-grid wakes for the WRF model, Wind Energy, 25, 1573–1595, https://doi.org/10.1002/we.2758, 2022.
- Macdonald, R. W.: Modelling the mean velocity profile in the urban canopy layer, Bound.-Lay. Meteorol., 97, 25–45, https://doi.org/10.1023/A:1002785830512, 2000.
 - Mahrt, L., Vickers, D., Sun, J., Jensen, N. O., Jørgensen, H., Pardyjak, E., and Fernando, H.: Determination of the surface drag coefficient, Bound.-Lay. Meteorol., 99, 249–276, https://doi.org/10.1023/A:1018915228170, 2001.
 - Mauder, M., Ibrom, A., Wanner, L., De Roo, F., Brugger, P., Kiese, R., and Pilegaard, K.: Options to correct local turbulent flux measurements for large-scale fluxes using an approach based on large-eddy simulation, Atm. Meas. Tech., 14, 7835–7850, https://doi.org/10.5194/amt-14-7835-2021, 2021.
 - Metzger, S., Ayres, E., Durden, D., Florian, C., Lee, R., Lunch, C., Luo, H., Pingintha-Durden, N., Roberti, J. A., SanClements, M., et al.: From NEON field sites to data portal: A community resource for surface–atmosphere research comes online, Bull. Am. Meteor. Soc., 100, 2305–2325, https://doi.org/10.1175/BAMS-D-17-0307.1, 2019.
- Mohandes, M. A. and Rehman, S.: Wind speed extrapolation using machine learning methods and LiDAR measurements, IEEE Access, 6, 77 634–77 642, https://doi.org/10.1109/ACCESS.2018.2883677, 2018.
 - Monin, A. and Obukhov, A.: Basic Laws of Turbulent Mixing in the Atmosphere Near the Ground, Tr. geofiz. inst. AN SSSR 24, 163, 1954. NEON: National Ecological Observatory Network, 2D wind speed and direction (DP1.00001.001) Release 2025, https://data.neonscience.org/data-products/DP1.00001.001, 2025a.
- NEON: National Ecological Observatory Network, Eddy covariance data product (DP4.00200.001) Release 2025, https://data.neonscience.org/data-products/DP4.00200.001, 2025b.
 - Newman, J. F. and Klein, P. M.: The impacts of atmospheric stability on the accuracy of wind speed extrapolation methods, Resources, 3, 81–105, https://doi.org/10.3390/resources3010081, 2014.
 - Novick, K. A., Biederman, J. A., Desai, A. R., Litvak, M. E., Moore, D. J. P., Scott, R. L., and Torn, M. S.: The AmeriFlux network: A coalition of the willing, Agr. Forest Meteorol, 249, 444–456, https://doi.org/10.1016/j.agrformet.2017.10.009, 2018.
- Nygaard, N. G., Poulsen, L., Svensson, E., and Pedersen, J. G.: Large-scale benchmarking of wake models for offshore wind farms, J. Phys. Conf. Ser., 2265, 022 008, https://doi.org/10.1088/1742-6596/2265/2/022008, 2022.
 - Optis, M., Bodini, N., Debnath, M., and Doubrawa, P.: New methods to improve the vertical extrapolation of near-surface offshore wind speeds, Wind Energy Sci., 6, 935–948, https://doi.org/10.5194/wes-6-935-2021, 2021.
 - Päschke, E., Leinweber, R., and Lehmann, V.: An assessment of the performance of a 1.5 μm Doppler lidar for operational vertical wind profiling based on a 1-year trial, Atm. Meas. Tech., 8, 2251–2266, https://doi.org/10.5194/amt-8-2251-2015, 2015.
 - Peterson, E. W. and Hennessey Jr, J. P.: On the use of power laws for estimates of wind power potential, J. Appl. Meteorol. Climatol., 17, 390–394, https://doi.org/10.1175/1520-0450(1978)017<0390:OTUOPL>2.0.CO;2, 1978.
 - Pratt, J. W. and Gibbons, J. D.: Concepts of Nonparametric Theory, Springer Series in Statistics, Springer New York, ISBN 978-1-4612-5933-6 978-1-4612-5931-2, https://doi.org/10.1007/978-1-4612-5931-2, ISSN: 0172-7397, 1981.
- Pryor, S. C., Shepherd, T. J., Bukovsky, M., and Barthelmie, R. J.: Assessing the stability of wind resource and operating conditions, J. Phys. Conf. Ser., 1452, 012 084, https://doi.org/10.1088/1742-6596/1452/1/012084, 2020.





- Richardson, A. D., Hufkens, K., Milliman, T., Aubrecht, D. M., Chen, M., Gray, J. M., Johnston, M. R., Keenan, T. F., Klosterman, S. T., Kosmala, M., et al.: Tracking vegetation phenology across diverse North American biomes using PhenoCam imagery, Sci. Data, 5, 1–24, https://doi.org/10.1038/sdata.2018.28, 2018.
- Rogers, A. L., Rogers, J. W., and Manwell, J. F.: Comparison of the performance of four measure–correlate–predict algorithms, J. Wind Eng. Ind. Aerod., 93, 243–264, https://doi.org/10.1016/j.jweia.2004.12.002, 2005.
 - Ryu, K.-W., Kim, J.-Y., and Chamorro, L. P.: Vertical extrapolation of Weibull parameters using PDF scaling and wind shear exponent, J. Renewable Sustainable Energy, 17, https://doi.org/10.1063/5.0248532, 2025.
- Scheurich, F., Enevoldsen, P. B., Paulsen, H. N., Dickow, K. K., Fiedel, M., Loeven, A., and Antoniou, I.: Improving the accuracy of wind turbine power curve validation by the rotor equivalent wind speed concept, J. Phys. Conf. Ser., 753, 072 029, https://doi.org/10.1088/1742-6596/753/7/072029, 2016.
 - Segalini, A., Fransson, J. H. M., and Alfredsson, P. H.: Scaling laws in canopy flows: a wind-tunnel analysis, Bound.-Lay. Meteorol., 148, 269–283, https://doi.org/10.1007/s10546-013-9813-2, 2013.
 - Solbakken, K., Birkelund, Y., and Samuelsen, E. M.: Evaluation of surface wind using WRF in complex terrain: Atmospheric input data and grid spacing, Environ. Modell. Software, 145, 105 182, https://doi.org/10.1016/j.envsoft.2021.105182, 2021.
 - Stehly, T., Duffy, P., and Mulas Hernando, D.: Cost of Wind Energy Review: 2024 Edition, Tech. rep., National Renewable Energy Laboratory (NREL), Golden, CO (United States), https://doi.org/10.2172/2479271, 2024.
 - Van Sark, W. G. J. H. M., Van der Velde, H. C., Coelingh, J. P., and Bierbooms, W. A. A. M.: Do we really need rotor equivalent wind speed?, Wind Energy, 22, 745–763, https://doi.org/10.1002/we.2319, 2019.
- Van Wijk, A. J. M., Beljaars, A. C. M., Holtslag, A. A. M., and Turkenburg, W. C.: Evaluation of stability corrections in wind speed profiles over the North Sea, J. Wind Eng. Ind. Aerodyn., 33, 551–566, https://doi.org/10.1016/0167-6105(90)90007-Y, 1990.
 - Wharton, S., Newman, J. F., Qualley, G., and Miller, W. O.: Measuring turbine inflow with vertically-profiling lidar in complex terrain, J. Wind Eng. Ind. Aerodyn., 142, 217–231, https://doi.org/10.1016/j.jweia.2015.03.023, 2015.
- Wharton, S., Ma, S., Baldocchi, D. D., Falk, M., Newman, J. F., Osuna, J. L., and Bible, K.: Influence of regional nighttime atmospheric regimes on canopy turbulence and gradients at a closed and open forest in mountain-valley terrain, Agric. For. Meteorol., 237, 18–29, https://doi.org/10.1016/j.agrformet.2017.01.020, 2017.
 - Wharton, S., Puccioni, M., De Wekker, S. F., Oldroyd, H., Miksch, M., Schroeder, M., Arthur, R. S., and Fast, J. D.: An overview of DOE's tall turbines onshore field campaigns: Using Doppler lidar to provide new insights into the wind resource over forests, 2024.
- Wiersema, D. J., Lundquist, K. A., and Chow, F. K.: Mesoscale to microscale simulations over complex terrain with the immersed boundary method in the weather research and forecasting model, Mon. Weather Rev., 148, 577–595, https://doi.org/10.1175/MWR-D-19-0071.1, 2020.
 - Wise, A. S., Neher, J. M. T., Arthur, R. S., Mirocha, J. D., Lundquist, J. K., and Chow, F. K.: Meso-to micro-scale modeling of atmospheric stability effects on wind turbine wake behavior in complex terrain, Wind Energy Sci., 7, 368–386, https://doi.org/10.5194/wes-7-367-2022, 2021.
- Wiser, R., Millstein, D., Hoen, B., Bolinger, M., Gorman, W., Rand, J., Barbose, G., Cheyette, A., Darghouth, N., Jeong, S., Kemp, J., O'Shaughnessy, E., Paulos, B., and Seel, J.: Land-based wind market report: 2024 edition, Lawrence Berkeley National Laboratory, https://eta-publications.lbl.gov/sites/default/files/2024-09/land-based_wind_market_report_2024_edition.pdf, 2024.
 - Yi, C.: Momentum transfer within canopies, J. Appl. Meteorol. Climatol., 47, 262-275, https://doi.org/10.1175/2007JAMC1667.1, 2008.